

# NOAA NESDIS STAR

ALGORITHM THEORETICAL BASIS DOCUMENT

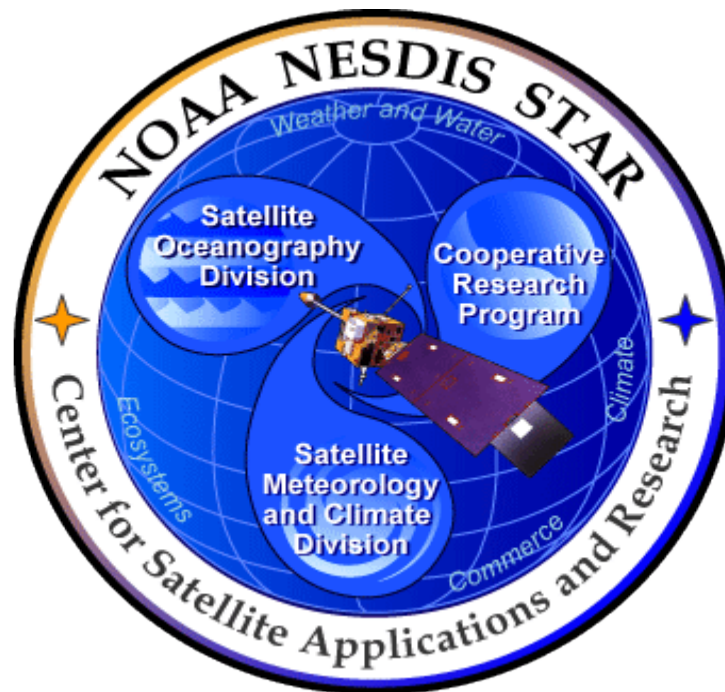
Version: 1.0

Date: January 17, 2012

TITLE: GOES LST Algorithm Theoretical Basis Document

Page 2 of 81

---



## NOAA NESDIS CENTER FOR SATELLITE APPLICATIONS AND RESEARCH

### GOES IMAGER LAND SURFACE TEMPERATURE ALGORITHM THEORETICAL BASIS DOCUMENT

Version 3.0

# NOAA NESDIS STAR

ALGORITHM THEORETICAL BASIS DOCUMENT

Version: 1.0

Date: January 17, 2012

TITLE: GOES LST Algorithm Theoretical Basis Document

Page 3 of 81

---

TITLE: GOES LST ALGORITHM THEORETICAL BASIS DOCUMENT VERSION 3.0

AUTHORS:

Donglian Sun (GMU/COS/GGS)

Li Fang (GMU/COS/GGS)

Yunyue Yu (NOAA/NESDIS/STAR)

## GOES LST ALGORITHM THEORETICAL BASIS DOCUMENT VERSION HISTORY SUMMARY

Version	Description	Revised Sections	Date
1.0	New document adapted from STAR EPL guidelines for GOES LST PDR	New Document	1/31/2011
2.0	Revised by D. Sun,L. Fang and Y. Yu for CDR	3.1, 3.2, 3.3, 3.5, 4.1	5/12/2011
3.0	Revised by D. Sun,L. Fang and Y. Yu for SRR		1/7/2012

## VERSION 2.0 CHANGES

Section	Page	Revision
3.1	19	Input format changed to HDF4
3.2.3	21	IMS snow/ice mask used for QC purposes only
3.3.1	23	Two-channel renamed-Dual Window
3.3.3.1	30	Section header changed for clarity
3.5.2.1	52	Two-channel renamed Dual-Window
3.5.2.2	53, 57	Two-channel renamed Dual-Window
4.1	65	GSIP input assumptions revised

# NOAA NESDIS STAR

ALGORITHM THEORETICAL BASIS DOCUMENT

Version: 1.0

Date: January 17, 2012

TITLE: GOES LST Algorithm Theoretical Basis Document

Page 4 of 81

---

---

## VERSION 3.0 CHANGES

<b>Section</b>	<b>Page</b>	<b>Revision</b>
3.5.2.2	63	GOES-MODIS LST retrieval comparisons removed
3.5.2.4	67-68	Added GOES LST accuracy/precision estimates from system test
3.7	73	Addition of GOES LST system test to validation

## TABLE OF CONTENTS

	<u>Page</u>
LIST OF FIGURES.....	8
LIST OF TABLES.....	10
LIST OF ACRONYMS.....	11
ABSTRACT .....	12
1. INTRODUCTION .....	14
1.1. Purpose of This Document.....	14
1.2. Who Should Use This Document.....	14
1.3. Inside Each Section.....	14
1.4. Revision History.....	15
2. SYSTEM OVERVIEW.....	16
2.1 Products Generated .....	16
2.2 Instrument Characteristics.....	17
2.3 Product Requirement.....	21
2.4 Retrieval Strategies .....	22
3. ALGORITHM DESCRIPTION.....	23
3.1 Processing Overview .....	23
3.2 Algorithm Input .....	25
3.2.1 Primary Sensor Data .....	26
3.2.2 Derived Sensor Data .....	26
3.2.3 Ancillary Data.....	27
3.2.4 Algorithm Coefficients and Control values.....	27
3.3 Theoretical Description.....	28
3.3.1 Physical Description .....	28
3.3.2 Mathematical Description of the LST Algorithm.....	30
3.3.2.1 Dual window algorithm.....	30

3.3.2.2 One-channel algorithm.....	35
3.3.2.3 Comparison with Split-Window Algorithms .....	37
3.3.3 Algorithm Selection.....	38
3.3.3.1 Forward Simulations .....	39
3.3.3.2 Coefficients Derivation .....	43
3.3.3.3 Simulation Analysis.....	45
3.3.3.4 Error Estimation .....	52
3.3.3.4.1 Water Vapor Uncertainty.....	52
3.3.3.4.2 Emissivity Uncertainty .....	54
3.3.3.5 Summary of Algorithm Selection.....	56
3.4 Algorithm Output .....	57
3.5 Performance Estimates .....	59
3.5.1 Test Data .....	59
3.5.1.1 GOES-imager Data.....	60
3.5.1.2 Ground Truth Data .....	62
3.5.1.2 Match-ups .....	63
3.5.2 Test with GOES-12 Observations.....	63
3.5.2.1 Comparison of Dual Window and Split Window Algorithms .....	63
3.5.2.2 Comparison of LSTs from GOES and MODIS .....	64
3.5.2.3 Precision and Accuracy Estimates.....	65
3.5.2.4 Performance Estimates from GOES LST system test.....	68
3.5.3 Test with GOES-13 Observations.....	69
3.5.3.1 The impacts of emissivity on GOES LST product.....	69
3.5.3.2 Comparison with the GSIP LST product .....	71
3.5.4 Error Budget.....	72
3.6 Practical Considerations.....	72
3.6.1 Numerical Computation Considerations .....	72
3.6.2 Programming and Procedural Considerations .....	73
3.6.2.1 Configuration of Retrieval.....	73
3.6.3 Quality Assessment and Diagnostics.....	73
3.6.4 Exception Handling.....	73

# NOAA NESDIS STAR

ALGORITHM THEORETICAL BASIS DOCUMENT

Version: 1.0

Date: January 17, 2012

TITLE: GOES LST Algorithm Theoretical Basis Document

Page 7 of 81

---

3.7 Validation.....	74
4. ASSUMPTIONS AND LIMITATIONS .....	75
4.1 Assumptions.....	75
4.2 Limitations .....	75
4.3 Potential Improvements.....	75
5. LIST OF REFERENCES .....	77

## LIST OF FIGURES

	<u>Page</u>
Figure 2.1. The transmittance (a) and temperature deficits ( $T_s-T_b$ ) (b) for the four infrared channels of the GOES 11 .....	19
Figure 2.2. Spectral distribution of the GOES-8 (similar to GOES-11) and GOES-12 (similar to GOES 13 and 14) imager channels.....	20
Figure 3.1. High Level Flowchart of the GOES LST retrieval .....	24
Figure 3.2. Atmospheric transmittance vs. wavelength for typical absorbing gases .....	29
Figure 3.3. ( $T_s-T_{11}$ ) vs. ( $T_{11}-T_{3.9}$ ) distribution .....	33
Figure 3.4. Radiative transfer simulation procedure.....	39
Figure 3.5. The 18 IGBP surface types used to match the full spectra of surface reflectance for forward GOES simulations. ....	41
Figure 3.6. The four GOES-13 imager infrared band spectral response functions super-imposed over the calculated high-res earth-emitted US Standard Atmosphere spectrum. ....	42
Figure 3.7. Procedure of the algorithm regression analyses.....	43
Figure 3.8. The standard deviation errors of LST retrieval from the GOES-13 simulations for the two proposed operational algorithms for daytime (left) and nighttime (right). ....	46
Figure 3.9. Bias errors (K) of the regression analysis for daytime (left) and nighttime (right).....	47
Figure 3.10. Standard deviation (STD) with water vapor bins are given for daytime (left) and nighttime (right). ....	48
Figure 3.11. Bias errors of the regression analysis with water vapor bins are given for daytime (left) and nighttime (right).....	49
Figure 3.12. The standard deviation errors of LST retrieval from the forward GOES simulations for the 9 inherited SW algorithms and their modified forms. ....	50
Figure 3.13. The standard deviation errors of LST retrieval from the forward GOES simulations for the 9 inherited SW algorithms and their modified forms. ....	51
Figure 3.14. Distributions of total column water vs. surface skin temperatures of the atmospheric profiles used in the simulation analyses (from Sun and Pinker, 2003) .....	53

# NOAA NESDIS STAR

ALGORITHM THEORETICAL BASIS DOCUMENT

Version: 1.0

Date: January 17, 2012

TITLE: GOES LST Algorithm Theoretical Basis Document

Page 9 of 81

---

Figure 3.15. Distributions of brightness temperature (BT) errors due to errors in surface emissivity from the GOES forward simulations .....	54
Figure 3.16. Spectral variation in surface emissivity for different surface types (from MOSART).....	55
Figure 3.17. LST derived from the GOES-12 observations on 07/31/2004 (upper) and 10/01/2004 (lower). .....	61
Figure 3.18. Scatter plots of LST derived from the GOES vs. in-situ observations for: (a) split-window algorithm, and (b) dual-window algorithm.....	64
Figure 3.19. Scatter plots of LST derived from GOES vs. SUFRAD observations.....	69

## LIST OF TABLES

	<u>Page</u>
Table 2.1. Spectral properties of GOES 12-14 Imager .....	21
Table 2.2. GOES LST requirements .....	21
Table 3.1. Input list of primary sensor data. ....	26
Table 3.2. Input list of derived sensor data. ....	27
Table 3.3 Input of ancillary data .....	27
Table 3.4. Candidate split window LST algorithms. ....	38
Table 3.5. Algorithm output data. ....	57
Table 3.6. Quality control flags at pixel level. ....	58
Table 3.7 Comparison of GOES-12 and GOES-13 imager channels .....	59
Table 3.8 SURFRAD Stations used for the algorithm validation. ....	62
Table 3.9 Seasonal Accuracy/Precision Estimations from GOES-12 LST Retrieval.....	65
Table 3.10 Statistics of LST retrieval accuracy and Precision .....	66
Table 3.11. Records with big errors from NCDC data (Cloud free && snow free).....	67
Table 3.12. Statistics of cloud cover pixels .....	68
Table 3.13 Statistics of snow cover pixels.....	68
Table 3.14 Statistics of LST retrieval accuracy after removing possible cloud contamination.....	68
Table 3.15. Emissivity dataset dependence of retrieval quality.....	70
Table 3.16. Difference between GOES LST and GSIP LST .....	71
Table 3.17. Comparison of GOES LST and GSIP LST against ground LST .....	71

---

---

## LIST OF ACRONYMS

ADP	Ancillary Data Processor
ADR	Ancillary Data Reader
ATBD	Algorithm Theoretical Base Document
CDR	Critical Design Review
CONUS	Continental United States
DF	Data Filter
DTR	Diurnal Temperature Range
FD	Full Disk
GLW	GOES LST Write
GOES	Geostationary Operational Environmental Satellite
GPR	GSIP Product Reader
GSIP	GOES Surface and Insolation Products
IMS	Interactive Multi-sensor snow and ice mapping System
IR	Infrared
LRA	LST Retrieval Algorithm
LST	Land Surface Temperature
MODIS	Moderate Resolution Imaging Spectroradiometer
NetCDF	Network Common Data Form
MSG	Meteosat Second Generation
NESDIS	National Environmental Satellite, Data, and Information Service
NOAA	National Oceanic and Atmospheric Administration
PDR	Preliminary Design Review
QC	Quality Control
QCF	Quality Control Flags
SAT	Surface Air Temperature
SWA	Software Architecture Document
TPW	Total Precipitable Water

### ABSTRACT

This Algorithm Theoretical Basis Document (ATBD) describes in detail the procedures for developing and using a land surface temperature (LST) algorithm designed for the GOES imager. It includes a description of the requirements and specifications of the LST products and some specific information about the GOES imager that is relevant to the derivation of the LST products. The main part of the ATBD is a description of the science of the proposed GOES imager LST algorithm. The process of algorithm selection is documented. This includes review of satellite LST research, selection of candidate algorithms and description of a large simulated GOES imager data set that was used to derive algorithm coefficients and test the candidate algorithms. The simulated radiances were calculated using sensor spectral response functions (SRF) that were available from the actual GOES imager instrument. A description of the expected implementation of the LST algorithm is provided. Ancillary data sets needed for the LST calculation are listed.

In this ATBD, while we mainly focus our efforts to derive LST products from the Imager of the GOES satellites currently in operational use, including GOES 12-14. Since at the time of this project development, GOES-11 was also in operational, to cover the possible reprocessing of GOES-11 data, this ATBD will cover LST product development for GOES 11-14 series. Two algorithms proposed for the GOES –M (12)-Q series will be tested and evaluated as the current GOES-imager LST algorithm. To cover the possible LST reprocessing for GOES imagers before GOES-12, nine split window algorithms, which are adapted from the literature and can be applied to GOES 8-11 imagers with split-window channels will also be evaluated. All algorithms used explicit spectral emissivity and satellite view angle information. Algorithm regression coefficients were derived from the simulation data set with new regression tree (RT) technique.

The selected algorithm was applied to the GOES imager data. Cloud mask of “clear” and “possible clear” are applied as a filter for cloud free conditions. The retrieved LSTs were compared against independent ground truth data and the results were analyzed. Comparisons of the dual-window algorithm with the split window algorithm are conducted. It is found the accuracy from the dual-window algorithm by combining middle infrared (MIR) with infrared window channel (11.0  $\mu\text{m}$ ) is worse than that from split-window algorithm, indicating the lack of split window in the GOES- M (12) –Q series may degrade the performance of GOES imager LST products. While all the algorithms are found to meet specs with the test data sets. Since GOES system consists of one satellite operating as GOES-East (GOES-E) in the eastern part of the constellation at 75° west longitude, and one satellite operating as GOES-West (GOES-W) at 135° west longitude, the viewing geometry may be quite different, to derive consistent land surface temperature across different

platforms, LSTs derived from the GOES-East and GOES-West are compared; moreover, comparison with polar orbiting system (MODIS) is also performed.

A process for routine evaluation of the operational GOES-imager LST is described, which includes automatic matchups against ground truth and methodology of the evaluation. Finally practical matters such as computer resources, instrument performance and its effects on the product are considered.

## 1. INTRODUCTION

The purpose, users, scope, related documents and revision history of this document are briefly described in this section. Section 2 gives an overview of the land surface temperature (LST) retrieval objectives and operations concept. Section 3 describes the baseline algorithm, its input data requirements, the theoretical background, sensitivity analyses and error budgeting. Test data sets and outputs are presented in Section 4. Some practical considerations are described in Section 5, followed by the assumptions and limitations associated with the algorithm in Section 6. Finally, Section 7 lists the references cited.

### 1.1. Purpose of This Document

This Algorithm Theoretical Basis Document (ATBD) explains the physical and mathematical background for an algorithm to derive LST product as part of the requirements for Imagers onboard the platform of the Geostationary Environmental Operational Satellite (GOES) series (GOES) of NOAA meteorological satellites. This document provides an overview of the required input data, the physical and mathematical backgrounds of the described algorithm and its predicted performance, sensitivity study of the algorithm, practical considerations, and assumptions and limitations.

### 1.2. Who Should Use This Document

The intended users of this document are those interested in understanding the physical bases of the LST algorithm and how to use the output of this algorithm for a particular application. This document also provides information useful to anyone maintaining or modifying the original algorithm.

### 1.3. Inside Each Section

This ATBD includes four sections:

Section 1.0 – Introduction provides the purpose, intended users, and revision history of the ATBD.

Section 2.0 – System Overview, describes the products generated by the algorithm and the characteristics of the instruments that supply inputs to the algorithm.

Section 3.0 - Algorithm Description, provides the algorithm details including a processing overview, input data, physical description, mathematical description, algorithm output, performance estimates, practical considerations, and validation.

Section 4.0 – Assumptions and Limitations, states assumptions presumed in determining that the software system architecture as designed will meet the requirements, and states limitations that may impact on the system’s ability to meet requirements.

Section 5.0 - List of References. gives a list of references cited in the document.

### **1.4. Revision History**

This is the third version (3.0) of the GOES LST ATBD produced for the GOES LST System Readiness Review (SRR).

Version 1.0 was produced, reviewed, and approved at the GOES LST Preliminary Design Review (PDR).

Version 2.0 was produced, reviewed, and approved at the GOES LST Critical Design Review (CDR).

## 2. SYSTEM OVERVIEW

This section describes objectives of the LST algorithm, details of the GOES imager instrument, and the product requirements.

### 2.1 Products Generated

Land surface temperature, a key indicator of the Earth surface energy budget, is widely required in applications of hydrology, meteorology and climatology. It is of fundamental importance to the net radiation budget at the Earth's surface and to monitoring the state of crops and vegetation, as well as important indicator of both the greenhouse effect and the energy flux between the atmosphere and earth surface (Norman & Becker, 1995; Li & Becker, 1993; Sellers *et al.*, 1998). Temperatures at the Earth's surface are important for the study of global warming. Typically, global temperature change is assessed by in situ surface air temperature (SAT) measurements at 2m height at weather stations. However, weather stations are usually located in relatively densely populated regions where anthropogenic impacts may affect measurements, and thus the temperature record may not be representative of global change. Moreover, station observations are sparse and unevenly distributed, and suffer from differences in elevation and time of observation (Peterson, 2003). The use of satellite-derived data could contribute to a large-area consistent measurement (Gallo *et al.*, 1999). Satellite LST can also be assimilated into climate, mesoscale atmospheric and land surface models to estimate sensible heat flux and latent heat flux. It can also be applied for analyzing climate change due to its rich archive from being routinely produced from imagery data of geostationary and polar-orbiting satellites.

Most satellite surface temperature products are based on polar orbiters, which cannot capture diurnal variations the LST particularly has. . Geostationary satellites with high temporal resolution provide an unique data source for deriving information on the diurnal LST cycle and diurnal temperature range (DTR) (Sun *et al.*, 2006) which is an important climate change index (Karl *et al.*, 1993).

Accuracy of the satellite LST measurement is limited by the atmospheric absorption, the complexity of surface emission characteristics, and sensor performance. Among those, variation of surface emissivity is the biggest difficulty in the satellite LST measurement. For the GOES LST, the accuracy requirement is 2.5 K for all the scanning modes (i.e., full disk, CONUS, and mesoscale). A primary objective of the GOES-Imager LST development team is to provide a state-of-the-art LST algorithm that meets the GOES-LST mission requirement.

Satellite retrievals of LST have been conducted for over forty years from a variety of polar-orbiting and geostationary satellites. For producing an LST climate data record from those programs, consistency of the LST products from different satellite mission is of importance. The GOES-Imager LST algorithm should have a good historical heritage for consistency among other satellite products.

Currently, surface emissivity variation is still the biggest impediment in satellite LST retrieval. The remote sensing community has been working for years to obtain a time series of accurate global land surface emissivity maps (e.g., Borbas *et al.*, 2008). The GOES-Imager LST algorithm should potentially benefit from such improvement of emissivity measurement.

Finally, algorithm simplicity and robustness is also a concern in order to produce the LST product as often as every thirty minutes which is the goal of GOES imager LST product refresh rate.

## 2.2 Instrument Characteristics

The Geostationary Operational Environmental Satellite (GOES) system, operated by the United States National Environmental Satellite, Data, and Information Service (NESDIS), supports weather forecasting, severe storm tracking, and meteorology research. Spacecraft and ground system work together to provide a continuous stream of environmental data. The National Weather Service (NWS) uses the GOES system for its United States operational weather forecasting and monitoring, and scientific researchers use the data to better understand land, atmosphere, ocean, and climate.

The GOES system uses geosynchronous satellites which—since the launch in 1974—have been a basic element of U.S. weather monitoring and forecasting. Designed to operate in geostationary orbit, 35,790 km (22,240 statute miles) above the earth, thereby remaining stationary with respect to a point on the ground, the advanced GOES I–M spacecraft continuously view the continental United States, observing environments of the Pacific and Atlantic Oceans, and Central, South America and southern Canada. The three-axis, body-stabilized spacecraft design enables the sensors to "stare" at the earth and thus more frequently image clouds, monitor earth's surface temperature and water vapor fields, and sound the atmosphere for its vertical thermal and vapor structures. Before being launched, GOES satellites are designated by letters (-A, -B, -C...). Once a GOES satellite is launched successfully, it is re-designated with a number (-1, -2, -3...) indicating its operational status. For instance, GOES-A to -F became GOES-1 to -6. Because GOES-G was a launch failure, it was never re-designated with a number. Since then, GOES-H -O became GOES-7 to GOES-14. Currently GOES-12 to -14 are in operations. GOES-11 is still available, but has been removed from the operational list.

In this ATBD, we mainly focus our efforts to derive the LST products from the Imager of the GOES satellites currently in operations:

- GOES-12 is designated GOES-South, currently located at 75°W over the Amazon River.
- GOES-13 is designated GOES-East, currently located at 105°W. It provides most of the U.S. weather information.
- GOES 14 was placed in orbit on 7 July 2009, underwent Post-Launch Testing until December 2009 and then was placed in on-orbit storage.

Since at the time of this project development, GOES-11 was operational, this ATBD will cover LST product development for GOES 11-14 series. The GOES imager is a multi-channel instrument designed to sense emitted and reflected energy from sampled areas of the earth. The multi-element spectral channels simultaneously sweep east west and west east along a north to south path using a two-axis mirror scan system.

The GOES imager before GOES-12, including GOES 8-11 series, had five channels centered at 0.67, 3.9, 6.7, 11 and 12  $\mu\text{m}$ , respectively. The 3.9, 11 and 12  $\mu\text{m}$  channels are infrared windows with little water vapor absorption, while the 6.7  $\mu\text{m}$  band is a water vapor band that can be used to detect atmospheric water vapor in the upper troposphere. The 0.67- $\mu\text{m}$  is a visible band that can be used to detect clouds during daytime.

The transmittance of the four thermal channels of GOES 11 vs. surface skin temperature distribution is shown in Figure 2.1(a).

The transmittance at the 6.7  $\mu\text{m}$  water vapor band is almost zero for skin temperature above 240 K. The surface radiation is almost totally absorbed by water vapor, so this band can be used to detect atmospheric water vapor distribution, but not for retrieving surface skin temperature.

The transmittances of the 11 and 12  $\mu\text{m}$  channels decrease significantly at high temperature (285-305 K); most values are below 0.8. This is why most existing split window algorithms that use the 11 and 12  $\mu\text{m}$  channels get larger errors at the warmer temperature range of 285-305K.

The transmittance for MIR channel 3.9  $\mu\text{m}$  is more stable, with less sensitivity to the surface skin temperature most values being above 0.8. Therefore, the MIR 3.9  $\mu\text{m}$  channel is a more appropriate window channel for retrieving LST than IR 11 and 12  $\mu\text{m}$  channels.

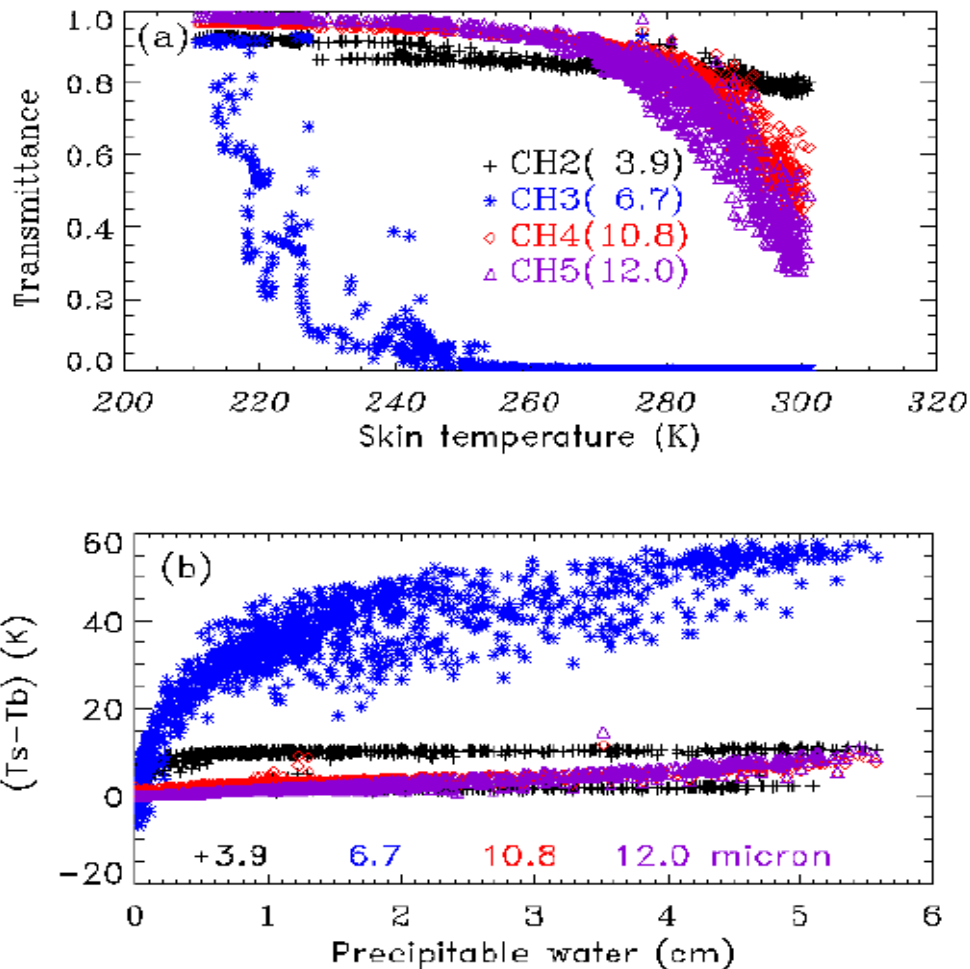


**Figure 2.1. The transmittance (a) and temperature deficits  $(T_s - T_b)$  (b) for the four infrared channels of the GOES 11**

Moreover, temperature deficit between skin temperature  $T_s$  and brightness temperature  $T_b$ ,  $(T_s - T_b)$  as shown in Figure 2.1(b), increases quickly at water vapor channel 6.7  $\mu\text{m}$ , and it can be as large as 60 K. Temperature deficit is relatively stable at window channels, it increases with water vapor at IR channels, but it almost doesn't change with water vapor amount at MIR channel. Therefore, it is best to use the MIR 3.9  $\mu\text{m}$  channel combined with the split window 11 and 12  $\mu\text{m}$  channels during nighttime, when the MIR channel does not contain solar energy reflected by surface.

The imagers on board the GOES M (12)-Q series, including the current operational GOES-13 and -14, don't have the 12- $\mu\text{m}$  channel (Figure 2.2), so it would not be possible to use the brightness temperature difference in the 11 and 12- $\mu\text{m}$  channels to correct for atmospheric effects. Attempts have been made to use ancillary data such as the total precipitable water and the characteristics of the middle-infrared channel of 3.9- $\mu\text{m}$  to correct for atmospheric effects.

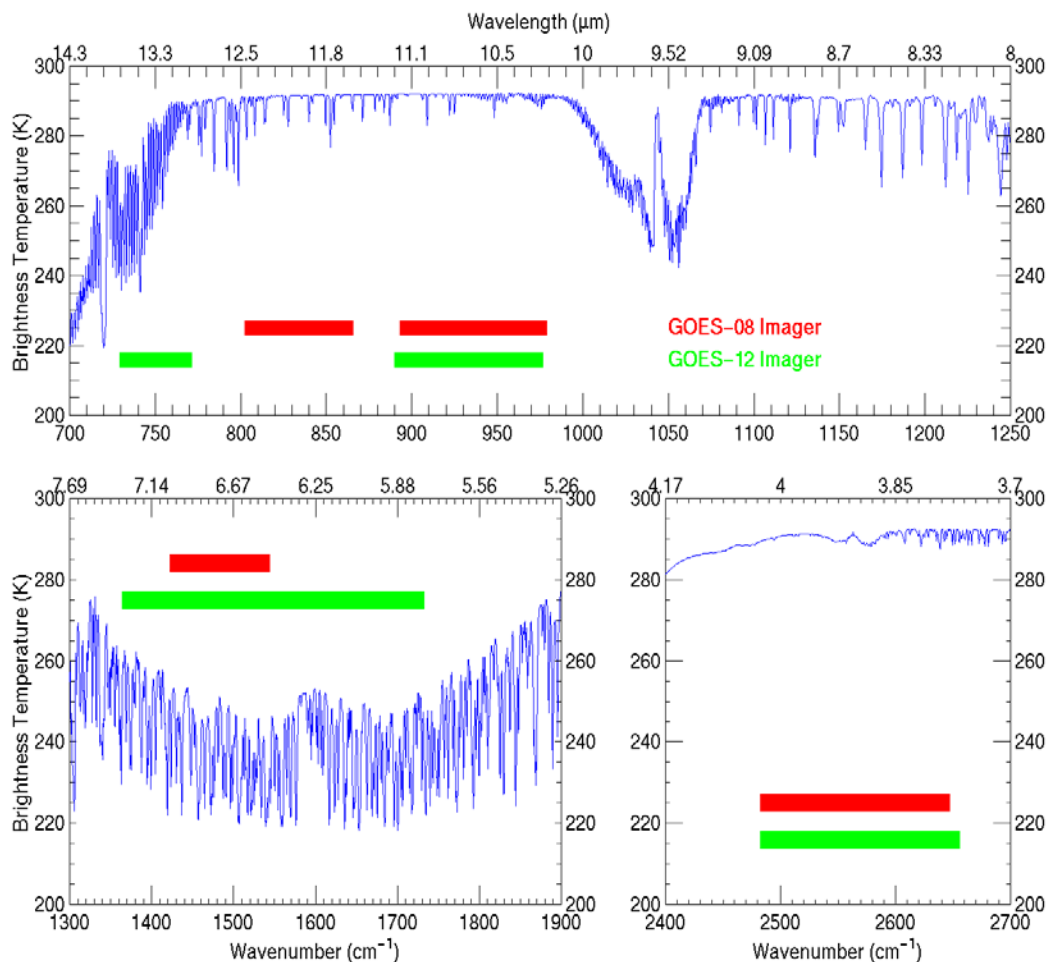


**Figure 2.2. Spectral distribution of the GOES-8 (similar to GOES-11) and GOES-12 (similar to GOES 13 and 14) imager channels**

The land surface temperature will be produced for each cloud free land pixel observed by the GOES sensor. The LST retrieval will rely on channels 2 and 4 of the current GOES-13 and -14 imager data (c.f. Table 2.1), using a dual window technique that is described in Section 3.

# NOAA NESDIS STAR

## ALGORITHM THEORETICAL BASIS DOCUMENT

Version: 1.0

Date: January 17, 2012

TITLE: GOES LST Algorithm Theoretical Basis Document

Page 21 of 81

**Table 2.1. Spectral properties of GOES 12-14 Imager**

Channels	Central Wavelength (μm)	Resolution (km <sup>2</sup> )
1 (visible)	0.65	1 km x 1km
2 (infrared)	3.9	4 km x 4km
3 (infrared)	6.75	4 km x 4km
4 (infrared)	10.7	4 km x 4km
6 (infrared)	13.3	4 km x 8 km (GOES-12/13) 4 km x 4km (GOES-14)

Shaded channels are used for LST retrieval.

### 2.3 Product Requirement

To make the consistency of LST product among different GOES platforms, we will follow the same requirement as those for GOES-R LST requirements of 2.3 K precision, which were originally defined in the mission requirement document (MRD), and further specified and updated in the Ground Segment Functional and Performance Specification (GS-F&PS). The requirements as of May, 2009 are listed in Table 2.2.

**Table 2.2. GOES LST requirements**

Observational Requirement	LEVEL <sup>1</sup>	Geographic Coverage <sup>2</sup>	Horiz. Res.	Mapping Accuracy	Msmnt. Range (K)	Msmnt. Accuracy <sup>3</sup> (K)	Msmnt. Precision (K)	Data Latency	Long-term StGOES imagery	Extent Qualifier <sup>4</sup>
LST (Skin): CONUS	T	C	4 km	4 km	210 – 350	2.5	2.3	60 min	TBD	LZA <70
LST (Skin): Hemispheric	T	FD	12 km	4 km	210 – 350	2.5	2.3	60 min	TBD	LZA <70

<sup>1</sup> T=target, G=goal

<sup>2</sup> C=CONUS, FD=full disk

<sup>3</sup> The measurement accuracy 2.3K is conditional with 1) known emissivity, 2) known atmospheric correction, and 3) 100% channel calibration accuracy; 5 K otherwise.

<sup>4</sup> LZA=local zenith angle

### 2.4 Retrieval Strategies

The GOES cloud mask from the GSIP dataset will be used for all cloud detection. LST retrieval in each scanning mode will be performed on each cloudless (i.e. “clear” and “possible clear” indicated by the cloud mask) land surface pixel, for day and night. A dual window technique will be applied for GOES 12-Q series with a switch to split-window type algorithm for the possible reprocessing of GOES imagers before GOES-12 for correcting atmospheric absorption in the radiative transfer process of the satellite signal. A specific path correction technique will be applied for better atmospheric correction. Coefficients of the retrieval algorithm will be stratified for different atmospheric conditions. The land surface emissivity information will be applied explicitly in the algorithm and a dynamic climatological emissivity data source will be used for such purpose. Finally, the LST retrieval quality will be indicated with a set of quality control flags which are either generated in the LST retrieval process or passed from the input data. The quality flags are assigned to each pixel.

## **3. ALGORITHM DESCRIPTION**

### **3.1 Processing Overview**

The processing outline of the LST is illustrated in Figure 3.1.

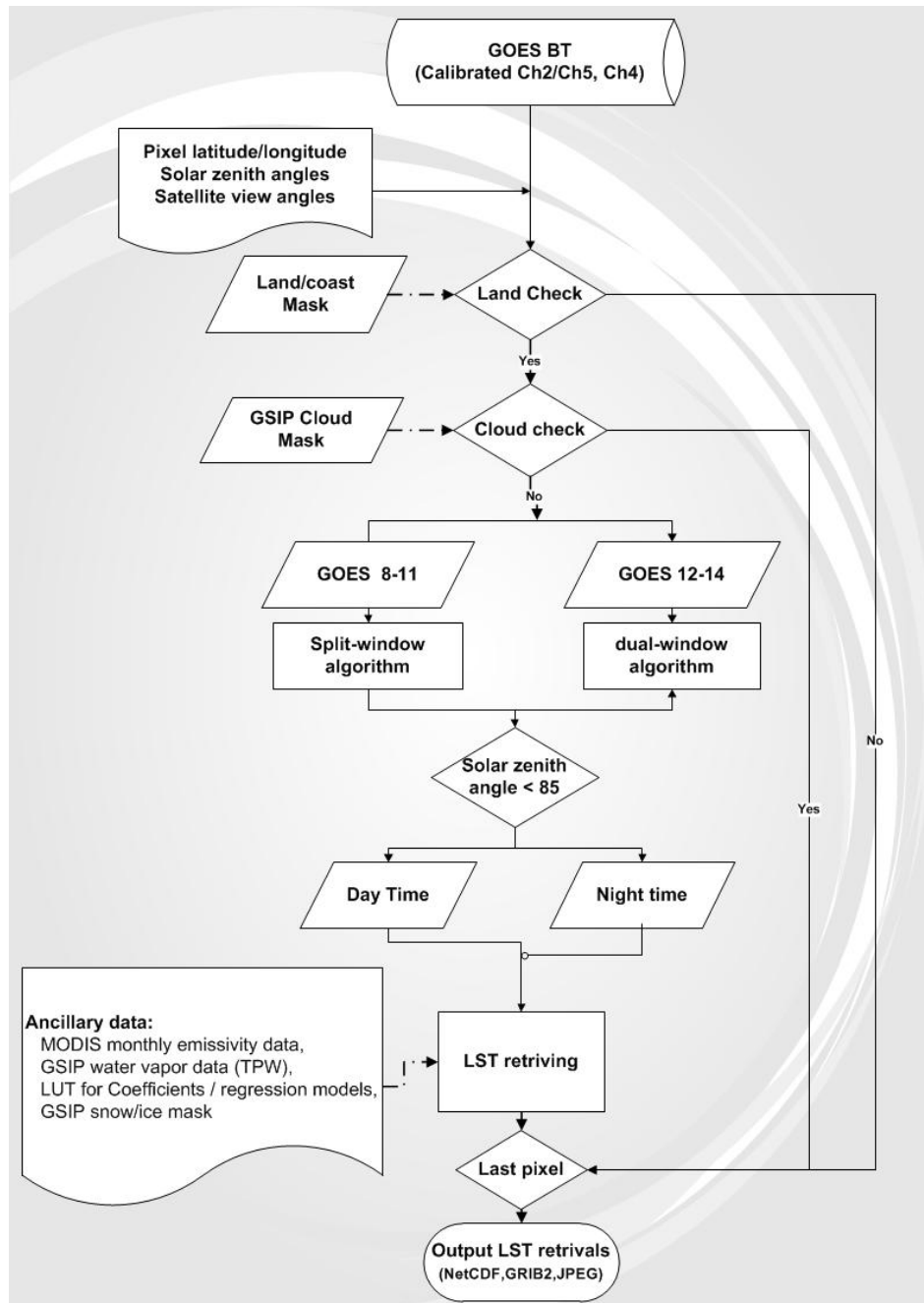


Figure 3.1. High Level Flowchart of the GOES LST retrieval

Major processing steps are:

- 1) Extract calibrated GOES imager sensor datasets including brightness temperatures, pixel geolocation, solar-target-sensor geometry, land/sea mask, sensor data quality control flags, cloud mask, snow fraction, water vapor, and aerosol optical depth from the GOES Surface and Insolation Products (GSIP).
- 2) Extract monthly emissivity, derived from MODIS
- 3) Geo-match the snow fraction, water vapor, and emissivity to the same pixel location as GOES imager pixels.
- 4) Label each pixel with land/ocean, coastal, cloud properties. Then filter the other data so that pixels labeled as ocean, coastal, cloudy, or probably cloudy are not processed.
- 5) Before calculating LST for each cloudless land pixel, day/night time flag is determined from the solar zenith angle of the sensor geometric data; and dry/moist atmospheric condition flag is determined using the GSIP water vapor information. LST of the pixel is calculated accordingly with the daytime/nighttime flags and dry/moist flags since the algorithm coefficients are stratified for each condition.
- 6) Set quality flags according to the original GOES imager data quality level, the condition of satellite view angle and cloud/snow/water vapor condition state.
- 7) The calculated LST values, their associated quality control flags, and pixel geo-location are combined with the LST product package and are written to files for user access.
- 8) The system output is written to files in NetCDF format and GRIB2 format. In addition, metadata is output to providing common information about the product and monitoring statistics of LST retrievals. JPEG files of LST retrieval imagery are generated for monitoring purposes.

### 3.2 Algorithm Input

This section describes the input needed to process the LST product. While the LST is derived for each pixel, ancillary datasets are required as well as the upstream GOES imager data.

### 3.2.1 Primary Sensor Data

The list below contains the primary sensor data used by the LST retrieval. By primary sensor data, we mean information that is derived solely from the GOES imager observations and geolocation information, or the level 1b data. Table 3.1 lists those input sensor data and their descriptions.

**Table 3.1. Input list of primary sensor data.**

Name	Type	Data Type	Description	Dimension
Ch2 ( or Ch5 for GOES 8-11) brightness temperature	Input	Short	Calibrated GOES Imager level 1b brightness temperatures at channel 2 for GOES 12-14 or channel 5 for GOES-11	Pixel resolution
Ch4 brightness temperature	Input	Short	Calibrated GOES Imager level 1b brightness temperatures at channel 4	Pixel resolution
Latitude	Input	Short	Pixel latitude	Pixel resolution
Longitude	Input	Short	Pixel longitude	Pixel resolution
Solar zenith	Input	Byte	GOES solar zenith angles	Pixel resolution
View zenith	Input	Byte	GOES view zenith angle	Pixel resolution
QC Flags	Input	Byte	GOES quality control flags	Pixel resolution

### 3.2.2 Derived Sensor Data

The GOES derived sensor data include: 1) land/coast mask, 2) cloud mask (indicating cloud condition as clear, probably clear, probably cloudy and cloudy), 3) snow fraction (<0.2 threshold value will be used to define snow free pixel), 4) water vapor (<=2.0g/cm<sup>2</sup> threshold value will be used to define dry atmosphere, >2.0g/cm<sup>2</sup> moist atmosphere, and >5.0g/cm<sup>2</sup> very moist), and 5) aerosol content (<0.3 threshold value will be used to define aerosol free).

Table 3.2 briefly describes input of the derived sensor data.

**Table 3.2. Input list of derived sensor data.**

Name	Type	Data Type	Description	Dimension
Land/coast mask	input	Byte	A land-ocean and coast mask	0.01 degree
Cloud mask	input	Byte	GSIP cloud mask data	Pixel resolution
snow fraction	input	Byte	GSIP snow mask	Grid
Water vapor	input	Float	GSIP water vapor	Grid

It is worth mentioning that the information on snow fraction and water vapor is used for the generation of quality control flags only. The detailed design of quality control flags is described in section 3.4.

### 3.2.3 Ancillary Data

The following table lists and briefly describes the ancillary data (emissivity data) required to run the LST.

**Table 3.3 Input of ancillary data**

Name	Type	Data Type	Description	Dimension
Emissivity	Input	Double	MODIS monthly emissivity, updated annually 1) GOES LST design allows for input and processing of MODIS monthly emissivity 2) GOES LST design allows for input and processing of a historical emissivity database	0.05 deg resolution

### 3.2.4 Algorithm Coefficients and Control values

In addition to the sensor data and the ancillary data, algorithm coefficients, regression tree models, lookup tables and some criterion values for algorithm selection and for quality control flags will be ingested as the input data.

---

### 3.3 Theoretical Description

The GOES LST algorithm development is based on a scientific research conducted by Sun and Pinker (2004) and Yu *et al.* (2008, 2009a). Theoretical details of the research are provided in this section.

#### 3.3.1 Physical Description

Under clear sky conditions, the outgoing spectral radiance at the top of the atmosphere can be represented as:

$$R(\lambda, \mu) = \varepsilon_0(\lambda, \mu)B(\lambda, T_s)\tau_0(\lambda, \mu) + R_a(\lambda, \mu) + R_s(\lambda, \mu, \mu_0, \varphi_0) + R_d(\lambda, \mu, \mu_0, \varphi_0) + R_r(\lambda, \mu) \quad (3.1)$$

Where  $\varepsilon_0$  is the surface spectral emissivity, B is the Plank function,  $\tau_0$  is the transmittance at the Earth's surface,  $R_a$  the thermal path radiance,  $R_s$  the path radiance resulting from scattering of solar radiation,  $R_d$  is the solar radiance and  $R_r$  the solar diffuse radiation and atmospheric thermal radiation reflected by the surface.  $T_s$  is the skin temperature,  $\lambda$  is the wavelength,  $\mu = \cos(\theta)$ ,  $\mu_0 = \cos(\psi)$ , where  $\theta$  is the satellite zenith angle,  $\psi$  the solar zenith angle,  $\varphi_0$  is the azimuth angle.

The wavelength  $\lambda$  is actually the wavelength center of a narrow interval because there is no way to measure the exact monochromatic signal as a continuous function of wavelength by satellite sensors. For the far-IR bands, solar contributions can be negligible, so the outgoing infrared spectral radiance at the top of atmosphere can be represented by:

$$R(\lambda, \mu) = \varepsilon_0(\lambda, \mu)B(\lambda, T_s)\tau_0(\lambda, \mu) + R_a(\lambda, \mu) \quad (3.2)$$

The purpose of the LST algorithm is to retrieve the land surface skin temperature  $T_s$  from the satellite sensor measured radiance  $R(\lambda, \mu)$ . Physically, in this problem, the surface temperature is basically coupled with two other factors: surface emissivity and the atmospheric absorptions. Developing an LST algorithm means to find a solution of decoupling the emissivity and the atmospheric absorption effects from satellite received radiance.

As shown from Figure 3.2, in order to retrieve surface information from satellite observations, we need to select window channels with no or less atmospheric absorption. Some bands, such as 3-4  $\mu\text{m}$ , 8-9  $\mu\text{m}$ , 10-12  $\mu\text{m}$ , are some typical atmospheric windows.

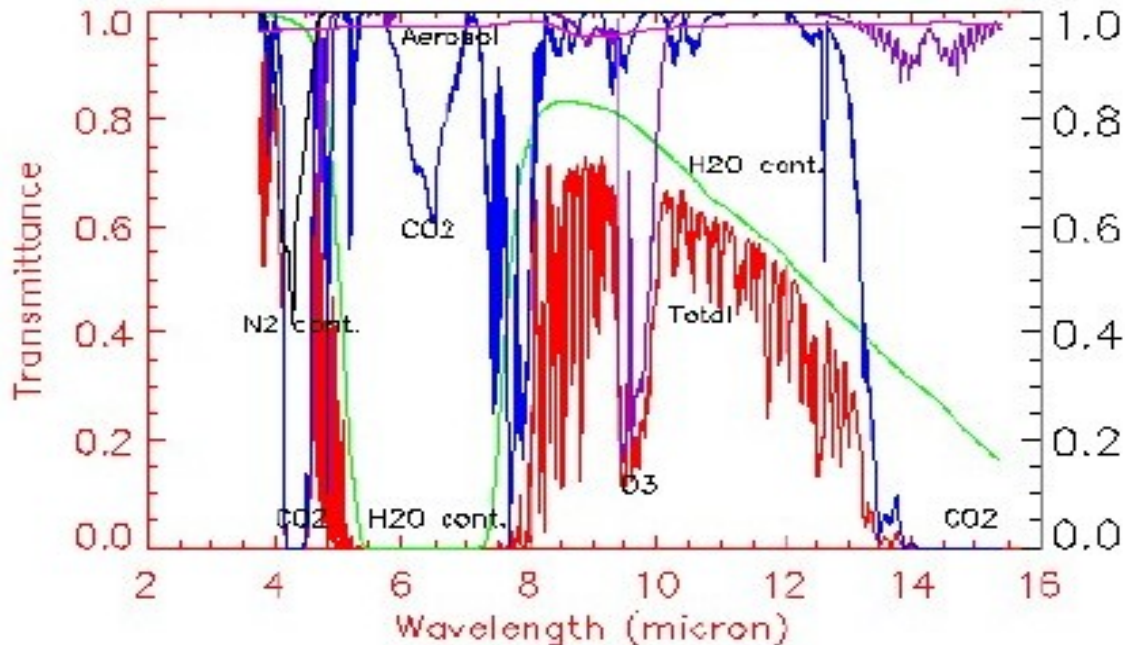


**Figure 4.2. Atmospheric transmittance vs. wavelength for typical absorbing gases**

An analytic solution to equation (3.1) is not easy, because the integration of the terms requires good knowledge of the atmospheric profiles which is not available in real time. In addition, land surface emissivity is coupled with the surface temperature in the equation, so the number of unknowns is always larger than the number of equations and this is the so-called ill-posed problem, even multiple channels of information are available. In the past thirty-five years, many approaches by using the two split window (SW) channels (11.0 and 12.0  $\mu\text{m}$ ) to the solution have been suggested (e.g., McMillin, 1975, Walton *et al.*, 1998), and widely used for producing the LST product (e.g., Prata, 1993 and 1994; Wan, 1999; Caselles *et al.*, 1997).

Since the operational GOES LST retrieval will be from current GOES imagers, including GOES-12, -13 and -14, there will be no 12.0  $\mu\text{m}$  channel, therefore, we cannot use split window channels to correct atmospheric effect. Sun and Pinker (2004) proposed a dual window algorithm by using the characteristics of the mid-infrared channel (3.9  $\mu\text{m}$ ) with less atmospheric (water vapor) absorption (Figure 2.1), and one channel (11  $\mu\text{m}$ ) plus water vapor correction algorithm.

Most SW algorithms explicitly use land surface emissivity values, while Sun and Pinker (1993; 1994) and Sikorsky *et al.* (2002) proposed emissivity information indirectly incorporated through the use of different coefficient sets determined by different land surface types. The latter approach must be tolerant to within-class emissivity variability and assume the land cover maps can be updated frequently, however, most available land cover products can only be available annually from EOS/MODIS and NOAA/AVHRR or seasonally from NPOESS/VIIRS, meanwhile emissivity maps that accommodate within class variability (Yu *et al.*, 2005) can be available more frequently from MODIS product. We expect that other emissivity map developments will be significantly improved by the launch of GOES-R in 2015. We therefore choose to use explicit emissivity approach.

### 3.3.2 Mathematical Description of the LST Algorithm

In the absence of the 12  $\mu\text{m}$  channel, we considered two candidate approaches:

- 1) Dual window algorithm combining 3.9 and 11.0  $\mu\text{m}$  channels
- 2) One-channel algorithm using total precipitable water (TPW)

#### 3.3.2.1 Dual window algorithm

The path thermal radiance in radiative transfer equation (3.1) is the vertically integrated effect of emission from every atmospheric layer modulated by the transmittance of the air above that emitting layer. It can be represented in spectral form as:

$$R_a(\lambda, \mu) = \int_{\tau_0}^1 B(\lambda, T_p) d\tau(\lambda, \mu, p) \quad (3.3)$$

Where  $B$ ,  $\lambda$ , and  $\mu$  are as given in equation (3.1),  $T_p$  is the air temperature (K) at vertical layer  $p$ ,  $p$  is the pressure of the vertical emitting layer (mb). Therefore, for the thermal infrared channel like 11.0  $\mu\text{m}$ , the outgoing infrared spectral radiance at the top of atmosphere can be represented in spectral form as:

$$R(\lambda, \mu) = \varepsilon_0(\lambda, \mu) B(\lambda, T_s) \tau_0(\lambda, \mu) + \int_{\tau_0}^1 B(\lambda, T_p) d\tau(\lambda, \mu, p) \quad (3.4)$$

However, for the middle infrared (MIR) 3.9  $\mu\text{m}$  channel, during nighttime the MIR radiance can be represented as the one in equation (3.4). But during daytime the solar radiation

reflected by the earth surface needs to be accounted for, and therefore the outgoing infrared spectral radiance at the top of atmosphere is represented as:

$$\begin{aligned}
 R(\lambda, \mu) = & \varepsilon_0(\lambda, \mu)B(\lambda, T_s)\tau_0(\lambda, \mu) + \int_{\tau_0}^1 B(\lambda, T_p)d\tau(\lambda, \mu, p) \\
 & + E_{solar} \cos \theta_s \frac{d_0^2}{d^5} \rho_b(\theta_s, \theta)\tau_0(\lambda, \mu)
 \end{aligned} \tag{3.5}$$

Where  $E_{solar}$  is the solar constant,  $d$  and  $d_0$  are the actual and mean earth-sun distances, respectively,  $\theta_s$  is solar zenith angle,  $\rho_b$  is the bidirectional reflectivity of the surface. During nighttime, the outgoing infrared spectral radiance at the top of atmosphere in both of the 11 and 3.9  $\mu\text{m}$  channels can be represented by equation (3.4). For a specific land surface type with surface emissivity close to unity, based on equation (3.4), the radiance error introduced by the atmosphere,  $\Delta R$ , can be represented as:

$$\begin{aligned}
 \Delta R = & B(\lambda, T_s) - R(\lambda, \mu) = B(\lambda, T_s) - B(\lambda, T_s)\tau_0(\lambda, \mu) - \int_{\tau_0}^1 B(\lambda, T_p)d\tau(\lambda, \mu, p) \\
 = & \int_{\tau_0}^1 B(\lambda, T_s)d\tau(\lambda, \mu, p) - \int_{\tau_0}^1 B(\lambda, T_p)d\tau(\lambda, \mu, p) \\
 = & \int_{\tau_0}^1 (B(\lambda, T_s) - B(\lambda, T_p))d\tau(\lambda, \mu, p)
 \end{aligned} \tag{3.6}$$

In the atmospheric window regions, the absorption is weak, so that:

$$\tau = e^{-k_\lambda u} \approx 1 - k_\lambda u \tag{3.7}$$

Where  $k_\lambda$  is the absorption coefficients at wavelength  $\lambda$ ,  $u$  is absorption gas optical path (mainly water vapor in window channel). Under this assumption, equation (3.6) can be rewritten as:

$$\Delta R \approx k_\lambda \int_0^{u_s} (B(\lambda, T_s) - B(\lambda, T_p)) du \approx \left. \frac{\partial B}{\partial T} \right|_{T_s} k_\lambda \int_0^{u_s} (T_s - T_p) du \tag{3.8}$$

$u_s$  is the total optical depth from the surface to the top of atmosphere. From the Planck function we get:

$$\Delta R = B(\lambda, T_s) - R(\lambda, \mu) = B(\lambda, T_s) - B(\lambda, T_\lambda) \approx \left. \frac{\partial B}{\partial T} \right|_{T_s} (T_s - T_\lambda) \quad (3.9)$$

where  $T_\lambda$  is brightness temperature at wavelength  $\lambda$ .

From (3.8) and (3.9) it follows that

$$T_s - T_\lambda = k_\lambda \int_0^{u_s} (T_s - T_p) dl \quad (3.10)$$

Using the two window channels 11.0 and 3.9  $\mu\text{m}$  (night), two such equations with different absorption coefficient  $k_\lambda$  can be solved simultaneously, to yield:

$$T_s - T_{11} = \left( \frac{k_{11}}{k_{3.9} - k_{11}} \right) (T_{11} - T_{3.9}) \quad (3.11)$$

Equation (3.11) is derived based on the assumption that surface emissivity is close to unity, and therefore it can be applied to any surface type, land as well as water, as long as the assumption is valid. However, the surface emissivities for some land surface types are not close to unity, in particular, in the 3.9  $\mu\text{m}$  channel. As shown in Figure 3.3, the relationship between the deficit of surface skin temperature and brightness temperature at 11  $\mu\text{m}$  ( $T_s - T_{11}$ ) and brightness temperature difference ( $T_{11} - T_{3.9}$ ) is nonlinear, so we propose to add an nonlinear term  $(T_{11} - T_{3.9})^2$ .

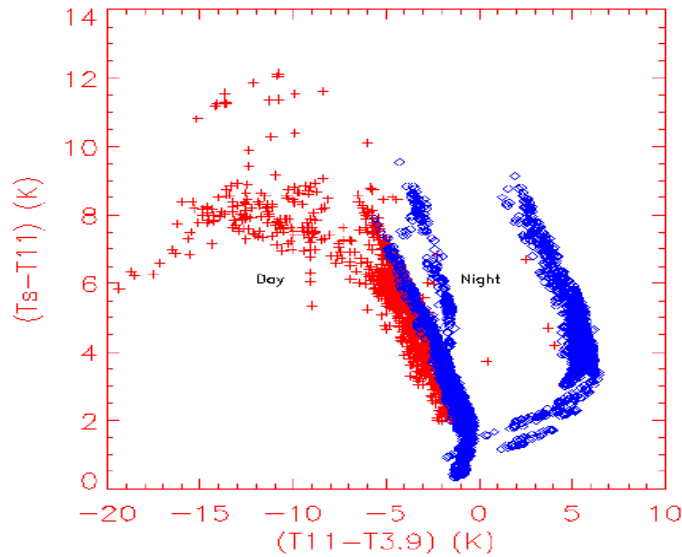


**Figure 5.3.  $(T_s - T_{11})$  vs.  $(T_{11} - T_{3.9})$  distribution**

In the figure,  $T_{11}$  and  $T_{3.9}$  are the GOES imager brightness temperature at channels 4 and 2,  $T_s$  is the skin temperature.

Moreover, we need to add some emissivity correction term. If the satellite viewing correction term  $(\sec\theta - 1)$  proposed by McClain et al. (1985) is added to the LST retrieval equation, during nighttime, we can get:

$$LST = a_0 + a_1 T_{11} + a_2 (T_{11} - T_{3.9}) + a_3 (T_{11} - T_{3.9})^2 + a_4 (1 - \varepsilon_{11}) + a_5 (\sec \theta - 1) \quad (3.12)$$

Where  $\varepsilon_{11}$  is the emissivity at 11  $\mu\text{m}$ .

However, during daytime, as shown in Figure 3.3, the brightness temperature deficits  $(T_{11} - T_{3.9})$  have large negative values. During daytime the brightness temperature in the middle infrared channel contains the solar radiation reflected by the earth surface, which makes  $T_{3.9}$  increase.

To reduce the solar signal contamination in the brightness temperature, the solar contribution should be subtracted from the observed middle infrared signal:

$$T'_{3.9} = T_{3.9} - f^{-1} \left( E_{solar} \cos \theta_s \frac{d_0^2}{d^2} \rho_b(\theta_s, \theta) \tau_0(\lambda, \mu) \right) \quad (3.13)$$

As the solar constant  $E_{solar}$  and sun-earth distance  $d$  are constant, for a specific surface type, the bidirectional effect depends on the solar zenith angle  $\theta_s$  and the satellite-viewing angle  $\theta$ . From equation (3.7), the surface transmittance  $\tau_0$  can be approximated as:

$$\tau_0(\lambda, \mu) \approx 1 - k_\lambda u_s \quad (3.14)$$

$u_s$  is the atmospheric total optical path,

$$u_s = \int_0^\infty \rho ds = \int_0^\infty \rho \sec \theta dz \quad (3.15)$$

$\rho$  is density of the atmospheric absorption gas,  $s$  is the geometry path,  $z$  is the height. Therefore, the solar correction term in equation (3.13) is a function of atmospheric total optical path  $u_s$ , satellite zenith angle  $\theta$ , and solar zenith angle  $\theta_s$ , given as:

$$\begin{aligned} T'_{3.9} &= T_{3.9} - f^{-1} \left( E_{solar} \cos \theta_s \frac{d_0^2}{d^2} \rho_b(\theta_s, \theta) \tau_0(\lambda, \mu) \right) \\ &\approx T_{3.9} - (c_0 + c_1 \rho_b(\theta_s, \theta) u_s \cos \theta_s) \end{aligned} \quad (3.16)$$

The coefficients in (3.16) may depend on surface type or emissivity, since the surface bidirectional reflectivity is related to it. If we assume Lambertian surface,  $\rho_b(\theta_s, \theta) = (1 - \varepsilon_0(\lambda, \mu))$ . In the window channels, the major absorbing gas is the water vapor, but neglect of absorption from  $CH_4$  and  $N_2O$  in the GOES imager 3.9  $\mu m$  channel can contribute to additional errors.

Estimating atmospheric  $CH_4$  and  $N_2O$  amounts is difficult. To allow for the effect of all absorbers in this channel, we propose to use the brightness temperature  $T_{3.9}$  to replace  $\rho_b(\theta_s, \theta) u_s$  in (3.16). (3.16) by modifying the coefficients in this equation as follows:

$$T'_{3.9} \approx T_{3.9} - (c_0'(l) + c_1'(l) T_{3.9} \cos \theta_s) \quad (3.17)$$

During daytime,  $T_{3.9}$  in equation (3.12) should be replaced by  $T'_{3.9}$ , therefore we have:

$$LST = a_0 + a_1 T_{11} + a_2 (T_{11} - T_{3.9}) + a_3 (T_{11} - T_{3.9})^2 + a_4 T_{3.9} \cos \theta_s + a_5 (1 - \varepsilon_{11}) + a_6 (\sec \theta - 1) \quad (3.18)$$

### 3.3.2.2 One-channel algorithm

In the atmospheric window channels, the water vapor absorption is weak. Therefore:

$$\tau_i = \exp(-k_i w \sec \theta) \approx 1 - k_i w \sec \theta \quad (3.19)$$

where  $i$  denotes the channel index,  $k_i$  is the absorption coefficient at channel  $i$ ,  $\theta$  is the satellite viewing angle, and  $w$  is the column water vapor. Hence

$$d\tau_i \approx -k_i \sec \theta dw \quad (3.20)$$

The measured radiance in the thermal window region can be expressed with respect to channel value from the radiative transfer equation (RTE) as:

$$\begin{aligned} R_i &= \varepsilon_i B_i(T_s) \tau_i + \int_0^\tau B_i(T_p) d\tau \\ &\approx \varepsilon_i B_i(T_s) (1 - k_i W \sec \theta) + k_i \sec \theta \int_0^W B_i(T_p) dw \end{aligned} \quad (3.21)$$

where  $B_i$  is the Plank function weighted for channel  $i$ ,  $T_i$  is the brightness temperature (K), measured at the satellite level in channel  $i$ ,  $T_s$  is the surface skin temperature (K),  $\varepsilon_i$  and  $\tau_i$  are the surface emissivity and atmospheric transmittance in channel  $i$ ,  $T_p$  is the air temperature (K) at vertical layer  $p$ ,  $p$  is the pressure of the vertical emitting layer (mb), and  $W$  represents the total precipitable water (TPW) (cm). Equation (3.21) is a simplification of equation (3.1), considering channel values instead of spectral values. Defining an atmospheric mean Planck radiance

$$B_i(T_a) = \int_0^W B(T_p) dw / \int_0^W dw \quad (3.22)$$

$T_a$  is the atmospheric mean temperature. Inserting equation (3.22) into equation (3.21) will yield:

$$R_i \approx \varepsilon_i B_i(T_s)(1 - k_i W \sec \theta) + k_i \sec \theta W B_i(T_a) \quad (3.23)$$

The Planck function can be expanded into a Taylor series about the brightness temperature  $T_i$  in the form of:

$$R_i = B_i(T_i) = \frac{DB}{DT} \Big|_{T_i} \frac{B(T_i)}{\frac{DB}{DT} \Big|_{T_i}} = \frac{DB}{DT} \Big|_{T_i} L(T_i)$$

$$B_i(T_s) \approx B_i(T_i) + \frac{DB}{DT} \Big|_{T_i} (T_s - T_i) = \frac{DB}{DT} \Big|_{T_i} (T_s - T_i + L(T_i)) \quad (3.24)$$

$$B_i(T_a) \approx B_i(T_i) + \frac{DB}{DT} \Big|_{T_i} (T_a - T_i) = \frac{DB}{DT} \Big|_{T_i} (T_a - T_i + L(T_i))$$

Inserting equation (3.24) into equation (3.23) will linearize the RTE with respect to temperature:

$$L(T_i) \approx \varepsilon_i(1 - k_i W \sec \theta)(T_s - T_i + L(T_i)) + k_i W \sec \theta(T_a - T_i + L(T_i)) \quad (3.25)$$

Several approximations have been proposed for  $L(T_i)$ . Sun and Pinker (2003) use:

$$L(T_i) \approx T_i / n_i \quad (3.26)$$

By inserting equation (3.26) into equation (3.25):

$$(C_{i1}T_i - \varepsilon_i T_s) = (T_a - \varepsilon_i T_s - C_{i2}T_i)k_i W \sec \theta \quad (3.27)$$

where

$$C_{i1} = \frac{1 + (n_i - 1)\varepsilon_i}{n_i}, C_{i2} = \frac{(n_i - 1)(1 - \varepsilon_i)}{n_i} \quad (3.28)$$

Let  $i$  represent the 11.0  $\mu\text{m}$  channel. For most land surfaces and the ocean, the emissivity at 11.0  $\mu\text{m}$  is essentially unity.

In order to reduce the number of unknown variables, we assume that the atmospheric mean temperature  $T_a$  is proportional to the surface temperature  $T_s$ ,

$$T_a \approx a_w T_s \quad (3.29)$$

It needs to be stated that assumption (3.29) may introduce errors if the surface emissivity at 11.0  $\mu\text{m}$  channel is not close to unity. A solution for  $T_s$  can be obtained as follows:

$$T_s \approx \frac{T_i}{[(a_w - 1)k_i W \sec \theta + 1]} = \frac{T_{11}}{c W \sec \theta + 1} \quad (3.30)$$

If we adopt emissivity correction to this equation, then:

$$LST = c_1 + c_2 T_{11} + c_3 W \sec \theta + c_4 (1 - \varepsilon_{11}) \quad (3.31)$$

### 3.3.2.3 Comparison with Split-Window Algorithms

As shown in Figure 3.1, for the possible reprocessing for GOES imager before GOES 12, we can use split-window algorithms. We also need to show the performance of the dual-window and one-channel algorithms as compared to the split-window type algorithms.

Table 3.4 lists the candidate split window LST algorithms. Each algorithm is composed of two parts: the base split window algorithm and path length correction (the last term in each algorithm). The base split window algorithms are adapted from those published split window algorithms as referred in the references, while the path length term is particularly added for additional atmospheric correction.

**Table 3.4. Candidate split window LST algorithms.**

No	Formula <sup>#</sup>	Reference
1	$T_s = C + (A_1 + A_2 \frac{1-\varepsilon}{\varepsilon} + A_3 \frac{\Delta\varepsilon}{\varepsilon^2})(T_{11} + T_{12})$ $+ (A_4 + A_5 \frac{1-\varepsilon}{\varepsilon} + A_6 \frac{\Delta\varepsilon}{\varepsilon^2})(T_{11} - T_{12}) + D(T_{11} - T_{12})(\sec \theta - 1)$	Wan & Dozier (1996); Becker & Li (1990).
2	$T_s = C + A_1 \frac{T_{11}}{\varepsilon} + A_2 \frac{T_{12}}{\varepsilon} + A_3 \frac{1-\varepsilon}{\varepsilon} + D(T_{11} - T_{12})(\sec \theta - 1)$	Prata & Platt (1991); modified by Caselles <i>et al.</i> (1997).
3	$T_s = C + A_1 T_{11} + A_2 (T_{11} - T_{12}) + A_3 (1 - \varepsilon_{11}) + A_4 \Delta\varepsilon$ $+ D(T_{11} - T_{12})(\sec \theta - 1)$	Coll & Valor (1997).
4	$T_s = C + A_1 T_{11} + A_2 (T_{11} - T_{12}) + A_3 \frac{1-\varepsilon}{\varepsilon} + A_4 \frac{\Delta\varepsilon}{\varepsilon^2} + D(T_{11} - T_{12})(\sec \theta - 1)$	Vidal (1991).
5	$T_s = C + A_1 T_{11} + A_2 (T_{11} - T_{12}) + A_3 (T_{11} - T_{12})\varepsilon_{11}$ $+ A_4 T_{12} \Delta\varepsilon + D(T_{11} - T_{12})(\sec \theta - 1)$	Price (1984).
6	$T_s = C + A_1 T_{11} + A_2 (T_{11} - T_{12}) + A_3 \varepsilon + D(T_{11} - T_{12})(\sec \theta - 1)$	Uliveri & Cannizzaro (1985).
7	$T_s = C + A_1 T_{11} + A_2 (T_{11} - T_{12}) + A_3 \varepsilon + A_4 \frac{\Delta\varepsilon}{\varepsilon}$ $+ D(T_{11} - T_{12})(\sec \theta - 1)$	Sobrino <i>et al.</i> (1994).
8	$T_s = C + A_1 T_{11} + A_2 (T_{11} - T_{12}) + A_3 (1 - \varepsilon) + A_4 \Delta\varepsilon + D(T_{11} - T_{12})(\sec \theta - 1)$	Ulivieri <i>et al.</i> (1992).
9	$T_s = C + A_1 T_{11} + A_2 (T_{11} - T_{12}) + A_3 (T_{11} - T_{12})(T_{11} - T_{12})$ $+ A_4 (1 - \varepsilon_{11}) + A_5 \Delta\varepsilon + D(T_{11} - T_{12})(\sec \theta - 1)$	Sobrino <i>et al.</i> (1993).

<sup>#</sup>Note:

$T_{11}$  and  $T_{12}$  represent the top-of-atmosphere brightness temperatures of GOES IMAGER channels 14 and 15, respectively;  $\varepsilon = (\varepsilon_{11} + \varepsilon_{12})/2$  and  $\Delta\varepsilon = (\varepsilon_{11} - \varepsilon_{12})$ , where  $\varepsilon_{11}$  and  $\varepsilon_{12}$  are the spectral emissivity values of the land surface at GOES IMAGER channels 14 and 15, respectively;  $\theta$  is the satellite view zenith angle

### 3.3.3 Algorithm Selection

To select a suitable algorithm for the GOES-imager, we analyzed the accuracy and sensitivity of the candidate algorithms using a comprehensive simulation dataset. The accuracy of the best performing algorithm was further studied using ground LST data from the SURFace RADiation (SURFRAD) network data and the corresponding GOES satellite imager data. We discuss these two analysis approaches in sequence below.

### 3.3.3.1 Forward Simulations

In order to derive regression coefficients in our algorithms, test and compare algorithm accuracy, we performed forward simulations using the latest version of (MODerate resolution atmospheric TRANsmission) (MODTRAN v4.3) to generate a comprehensive simulation dataset.

The MODTRAN atmospheric radiative transfer model (Berk et al., 2000) has been widely used in satellite remote sensing studies for about three decades. It is a moderate spectral resolution model, up to  $\text{cm}^{-1}$  in frequency. We used MODTRAN version 4, reversion 3, released in 2008. The radiative transfer simulation procedure is illustrated in Figure 3.4.

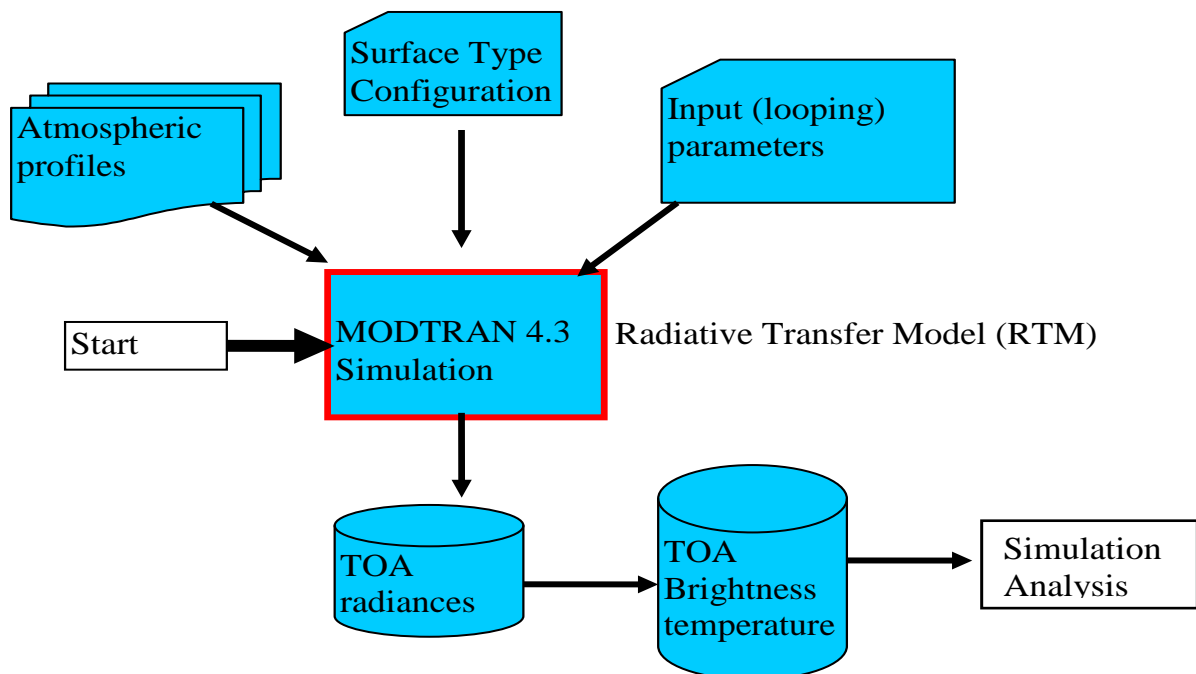


**Figure 3.6. Radiative transfer simulation procedure**

In order to account for the wide range of different atmospheric and surface conditions, a large number of simulations for each season need to be performed with variations in:

- Geometry of the problem (solar zenith angle, viewing and azimuth angles)
- Atmospheric conditions (profiles of ozone, water vapor, aerosols)

- 
- Surface conditions (spectral characteristics of the surface)
  - Characteristics of the instrument (spectral response of the satellite sensors); the current GOES imager spectral response functions were obtained from the NOAA/NESDIS (<http://www.oso.noaa.gov/goes/goes-calibration/goes-imager-srfs.htm>).

The latest version of MODTRAN 4.3 (MODerate resolution atmospheric TRANsmission) is used to perform forward simulations to GOES imager instruments and generate a simulation database. To make the simulations applicable to all possible conditions, the atmospheric (height, temperature and relative humidity) profiles with the matched surface height, pressure, temperature, and relative humidity from the Global NCEP Reanalysis (NRA) climatology (long-term mean) are used as the input.

In order to consider the seasonal variations, we performed simulations to four seasons using the NRA climatology data at winter (December-January-February mean), spring (March-April-May mean); summer: (June-July-August mean), and fall (September-October-November mean).

In order to represent the variability in solar geometry, the solar zenith angle (SZA) are calculated according to the latitude, longitude, Julian day, GMT time, thus the values at global coverage may vary from 0 to 180°.

To consider the effects of satellite zenith angles, simulations were performed for 5 zenith angle bins as satellite viewing zenith angle (VZA: 0, 2, 4, 6, 8), which is equal to satellite zenith angle (SZA: 0, 12.8, 26.38, 41.75, 62.44).

In order to make the GOES forward simulations applicable to different sensors with different spectral response functions (SRF), we have performed simulations to a wide spectral range from 3 to 14  $\mu\text{m}$  with 10  $\text{cm}^{-1}$  resolution. Therefore the input surface reflectance/emissivity are needed for full spectra but not for a spectral channel. The full spectra from 0.2 and 15  $\mu\text{m}$  at high spectral resolution (0.02  $\mu\text{m}$ ) for the IGBP surface types was modified and immigrated from the latest MODTRAN and MOSART emissivity database. The surface emissivity with full spectra from 0.2 to 15  $\mu\text{m}$  for 18 IGBP types, including the 17 MODIS IGBP types plus one surface type (Tundra) recommended by the JCSDA, . The total 18 IGBP types are shown in Figure 3.5.

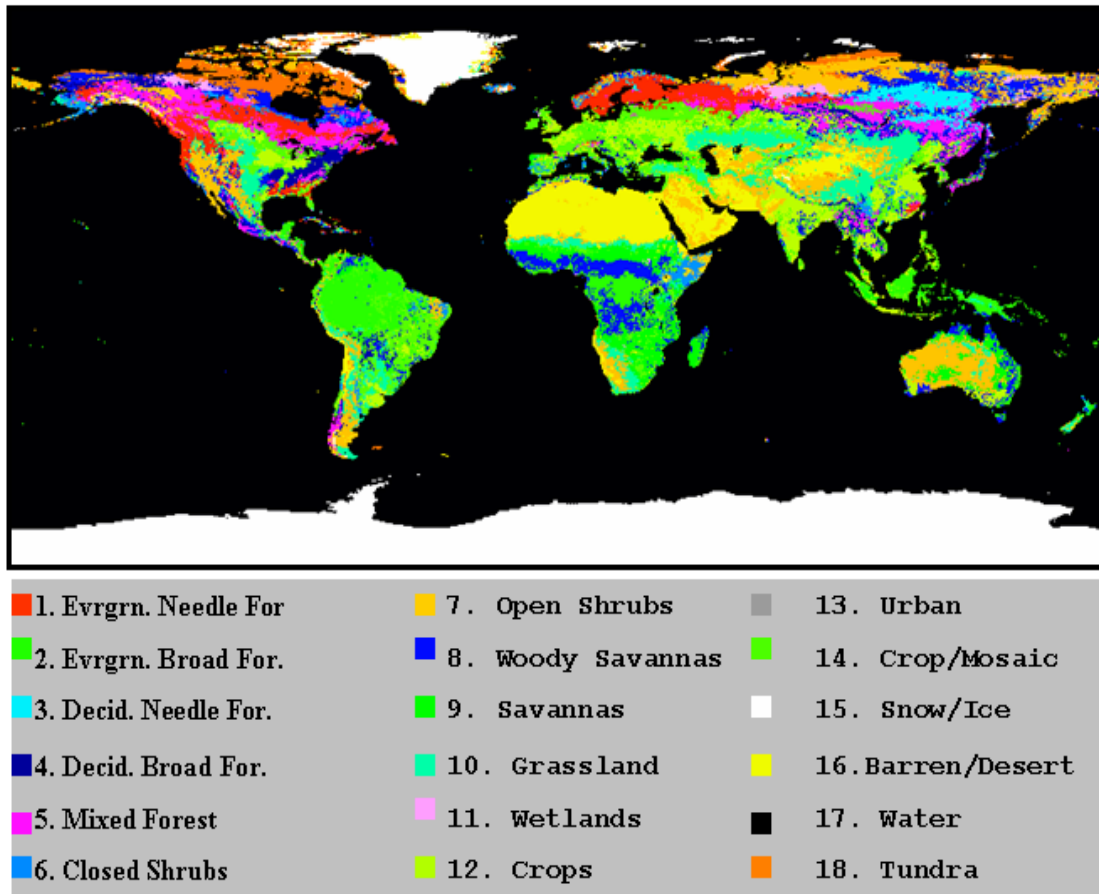


**Figure 3.7. The 18 IGBP surface types used to match the full spectra of surface reflectance for forward GOES simulations.**

We have completed this simulation database for testing and evaluation of LST algorithms. A total of 144 (cols) x 73 (rows) x 5 (satellite zenith angles) x 4 (seasons) simulation datasets were generated from the simulation process. The simulated datasets cover a wide range of spectrum from 3 to 14  $\mu\text{m}$ , with  $10 \text{ cm}^{-1}$  spectral resolution which can be used to simulate satellite sensor received radiances in different infrared channels.

The narrowband outgoing radiances at the TOA are obtained by convoluting the spectral radiances with the response function of the specific instrument.

$$I(\mu_0, \mu, \varphi) = \int_{\lambda_1}^{\lambda_2} L(\lambda) I_{\lambda}(\mu_0, \mu, \varphi) d\lambda \quad (3.32)$$

The radiance is then converted to reflectance. We first determined the mean channel radiance by integrating over the sensor spectral response function (SRF). The latest GOES-13 spectral response functions (Figure 3.6) from NOAA/NESDIS (<http://www.oso.noaa.gov/goes/goes-calibration/goes-imager-srfs.htm>) are used. The channel radiances were then converted into corresponding brightness temperatures.

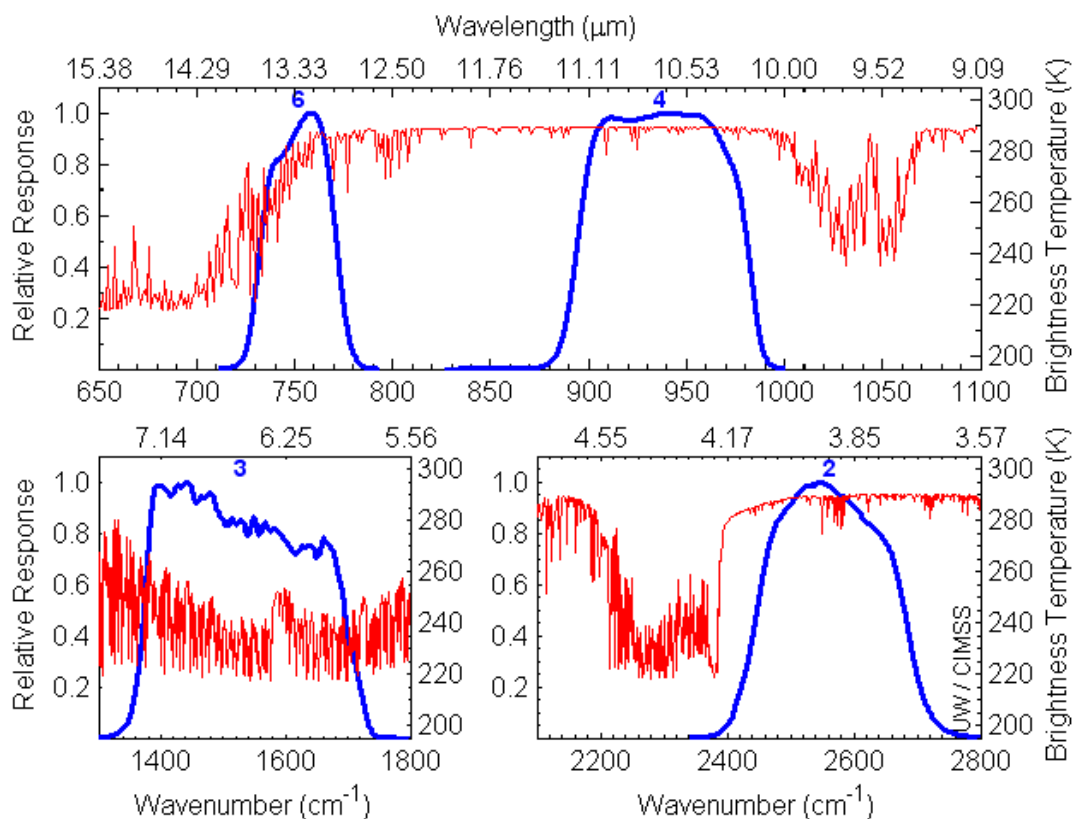


**Figure 3.8. The four GOES-13 imager infrared band spectral response functions super-imposed over the calculated high-res earth-emitted US Standard Atmosphere spectrum.**

Absorption due to carbon dioxide (CO<sub>2</sub>), water vapor (H<sub>2</sub>O), and other gases are evident in the high-spectral resolution earth-emitted spectrum.

### 3.3.3.2 Coefficients Derivation

Upon simulating the top-of-atmosphere radiances, we then conducted regression analyses and coefficients derivation for the algorithm development. The regression procedure and coefficients derivation process is illustrated in Figure 3.7.

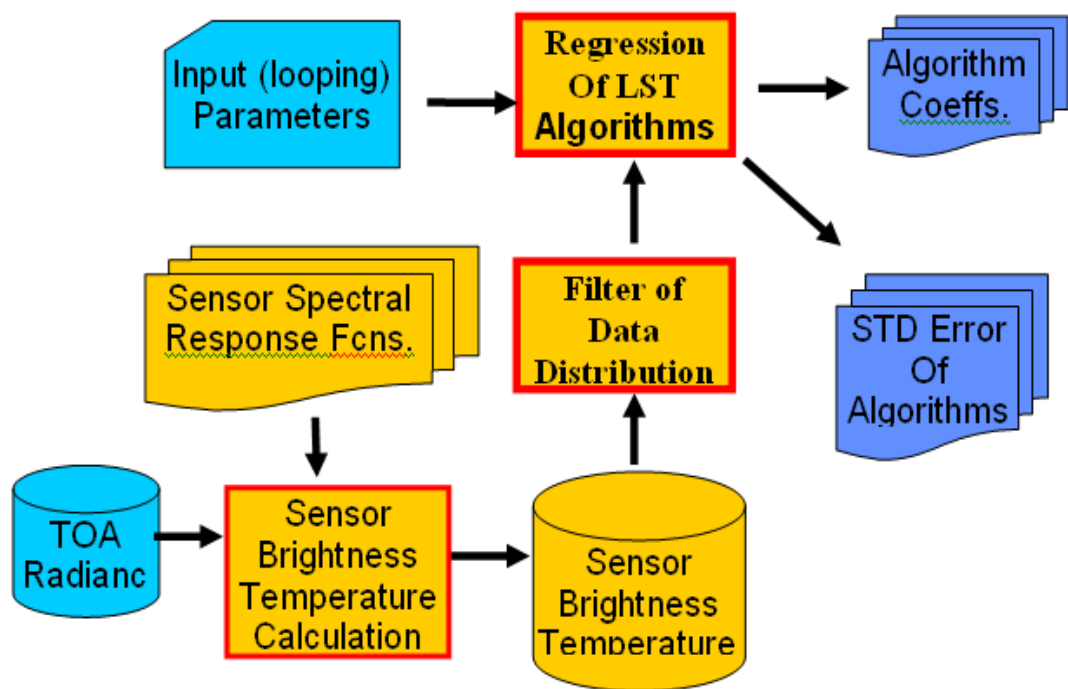


**Figure 3.9. Procedure of the algorithm regression analyses.**

We first performed convolution to calculate the mean channel radiance by integrating over the sensor spectral response function (SRF). The channel radiances were converted into corresponding brightness temperatures using the Planck function.

For most of the LST regression algorithms, the optimum coefficients have been determined by separating the ranges of parameters, such as atmospheric water vapor, boundary temperature and so on. The selection criteria and the boundary of the sub-ranges were made manually, mostly based on experience.

Take the generalized split-window algorithm as an example. Wan and Dozier (1996) extended the local split-window algorithm proposed by Becker and Li (1990) to a generalized split-window (GSW) algorithm by making the coefficients varying according to different conditions.

$$T_s = C + \left( A_1 + A_2 \frac{1 - \varepsilon}{\varepsilon} + A_3 \frac{\Delta \varepsilon}{\varepsilon^2} \right) (T_{11} + T_{12}) + \left( A_4 + A_5 \frac{1 - \varepsilon}{\varepsilon} + A_6 \frac{\Delta \varepsilon}{\varepsilon^2} \right) (T_{11} - T_{12}) + D(T_{11} - T_{12})(\sec \theta - 1) \quad (3.33)$$

Where  $T_{11}$  and  $T_{12}$  represent the top-of-atmosphere brightness temperature at around 11 and 12 microns, respectively;  $\varepsilon = \frac{\varepsilon_{11} + \varepsilon_{12}}{2}$  and  $\Delta \varepsilon = \varepsilon_{11} - \varepsilon_{12}$ ;  $\varepsilon_{11}$ ,  $\varepsilon_{12}$  are the emissivities at the two channels;  $\theta$  is the satellite view zenith angle;  $A_i (i = 1, 2, \dots, 6)$  and  $C$  are algorithm coefficients that depend on the spectral emissivities only.

In this GSW algorithm, Wan and Dozier (1996) made the coefficients in Becker and Li's local split-window algorithm changing according to some suggested initial guess values, or some kind of bins of 9 viewing angles (Cosine values of these angles are 0.415059, 0.445869, 0.475084, 0.529560, 0.626080, 0.713005, 0.781367, 0.966438, and 0.998631), 7 surface air temperatures (273, 281, 289, 295, 300, 305, 310), and 11 atmospheric column water vapor amount (0.5, 1.0, 1.5, 2.0, 2.5, 3.0, 3.5, 4.0, 4.5, 5.0, 5.5).

Because water vapor is the most significant atmospheric absorbing gas in the thermal window bands (Figure 3.2), the stratification according to water vapor amount acknowledges the capacity of warm atmospheres to hold more water vapor, and the degradation of LST algorithm performance is expected with increasing water vapor.

Due to significant differences in the discontinuity between LST and air temperature, during daytime and nighttime, many LST retrieval algorithms (or accompanying coefficient sets) were specified uniquely for daytime or nighttime use. However, how to determine these threshold values for different surface and atmospheric conditions may be the tricky part and mostly predefined based on experience.

Regression tree (RT) algorithm uses a piecewise regression technique which classifies the data into different subsets and yields different regression fits or models under different conditions. Through machine learning process, it can help us automatically find the threshold values, which is similar to the bins used in the GSW algorithm for stratification of different conditions (Sun and Yu, 2010; Sun et al., 2011). Therefore, instead of using traditional regression method, we will introduce RT algorithm for automatic determination of different surface and atmospheric conditions and the training of algorithm coefficients.

The Regression Tree (RT), as one of data mining tools, combines decision tree technique with traditional regression analysis, can provide flexible and robust analytical methods for identifying the relationships between complex environmental data (Breiman et al., 1984; De'ath and Fabricius, 2000). The basic strategy of decision tree algorithm is to select an attribute that will best separate the samples into individual classes by a measurement '*Information Gain Ratio*' based on information-theoretic 'entropy'. 'Best' means to find the minimum information needed to keep the least "impurity" of the partitions (Han and Kamber, 2001). The tree structure can be easily explained, and the process by which a particular decision "flows" through the decision tree can be readily shown.

The RT program constructs an unconventional type of tree structure, with the tree leaves containing linear regression models. RT technique provides robust tools to handle nonlinear relationship within large data sets. It can help us find the threshold values and rules automatically. By applying the rule induction techniques, it is possible to discern the conditions that lead to a relationship within computer-determined subsets of the data. The RT technique, such as the M5P, is a powerful tool for generating rule-based models that balance the need for accurate prediction against the requirements of intelligibility (Wang and Witten, 1997). The M5P algorithm, the most commonly used classifier of the RT family, builds regression trees whose leaves are composed of multivariate linear models and the nodes of the tree are chosen over the attribute that maximizes the expected error reduction as a function of the standard deviation of output parameter. Therefore, the M5P RT algorithm is adopted for automatic training of algorithm coefficients, and the determination of different surface and atmospheric conditions.

The RT algorithm will be run only for the training of algorithm coefficients. Through this RT training or machine learning process, a tree structure, which is composed of regression models under different conditions, can be obtained and used to replace the look up tables of traditional regression coefficients, for LST product generation.

### **3.3.3.3 Simulation Analysis**

One season (summer) has been tested for the two proposed algorithms for GOES 12-14 (operational algorithms) and for 9 previously published split window type (historical) algorithms and their modified (with zenith angle correction term) forms, totally 18 SW algorithms for possible reprocessing of LST from GOES imager before GOES-12.

For each of the tested algorithms, we calculate the bias and standard deviation of the regressions. Due to the high water vapor amount during summer, the LST retrieval errors in summer are usually larger than in other seasons. As shown in Figures 3.8-3.11, it is found

that the largest errors always appear at warm surface temperature above 280 K, and viewing zenith angle larger than 4 degree or satellite zenith angle greater than 41.75 degree.

To have a closer look at error distributions, we produced errors vs. viewing angles and skin temperature distributions of the regression fits for the two proposed operational algorithms for daytime and nighttime results.

Figures 3.8-3.9 show that the standard deviation and bias errors are usually larger during daytime than those during nighttime. This is because there is no or less solar contamination and less water vapor during nighttime.

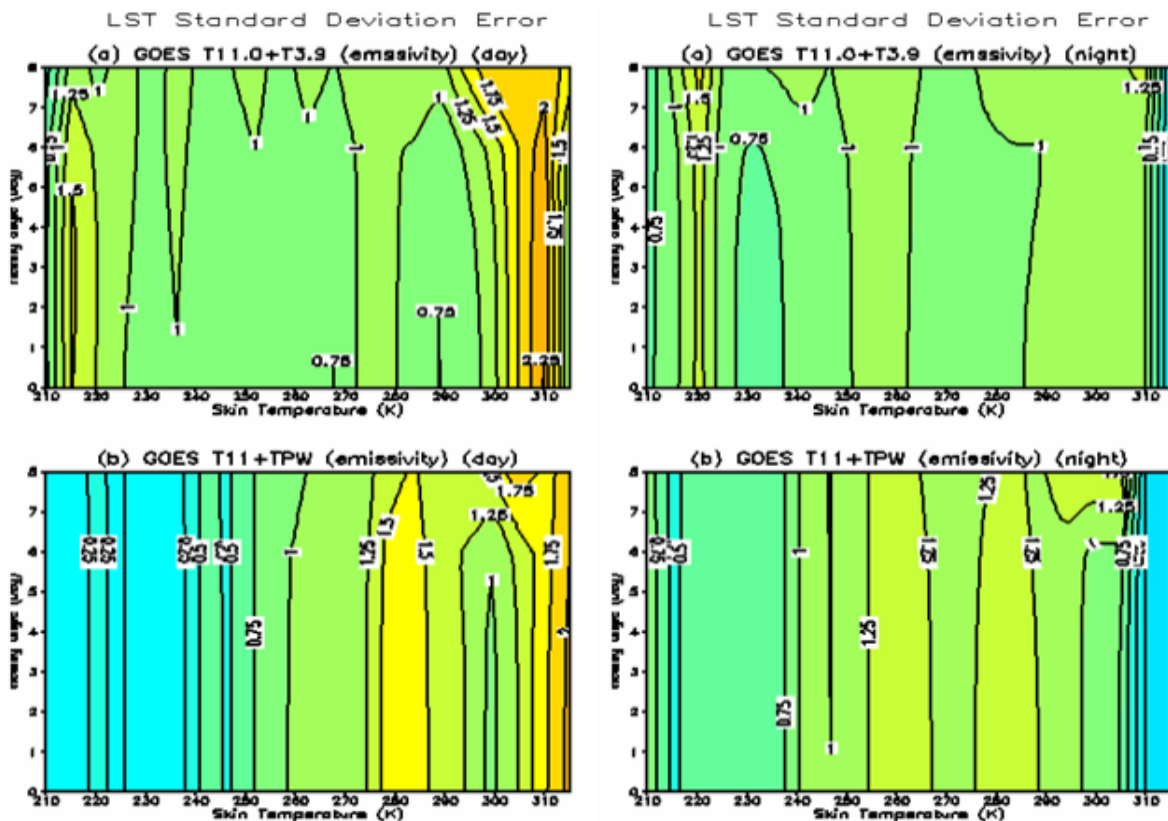
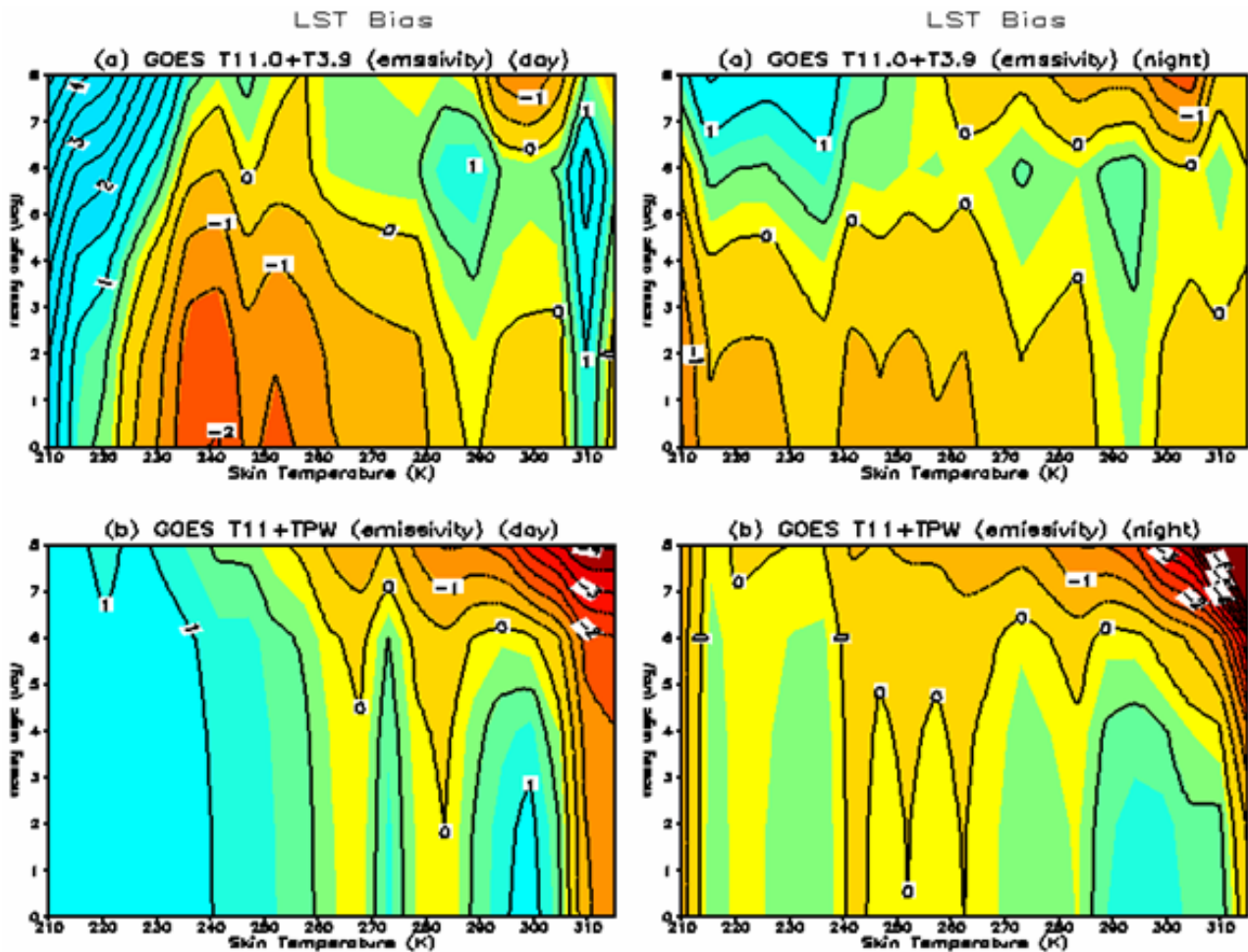


Figure 3.10. The standard deviation errors of LST retrieval from the GOES-13 simulations for the two proposed operational algorithms for daytime (left) and nighttime (right).



**Figure 3.11. Bias errors (K) of the regression analysis for daytime (left) and nighttime (right).**

Compared to split window type algorithms as shown in Figures 3.11-12, we can see both dual window (3.9+11  $\mu\text{m}$ ) algorithm and one-channel ( $T_{11}$ +TPW) algorithms show worse performance than the split-window type algorithms. Meanwhile, Figure 3.9 shows that the bias errors from dual-window algorithm are smaller than those from one-channel algorithm.

# NOAA NESDIS STAR

## ALGORITHM THEORETICAL BASIS DOCUMENT

Version: 1.0

Date: January 17, 2012

TITLE: GOES LST Algorithm Theoretical Basis Document

Page 48 of 81

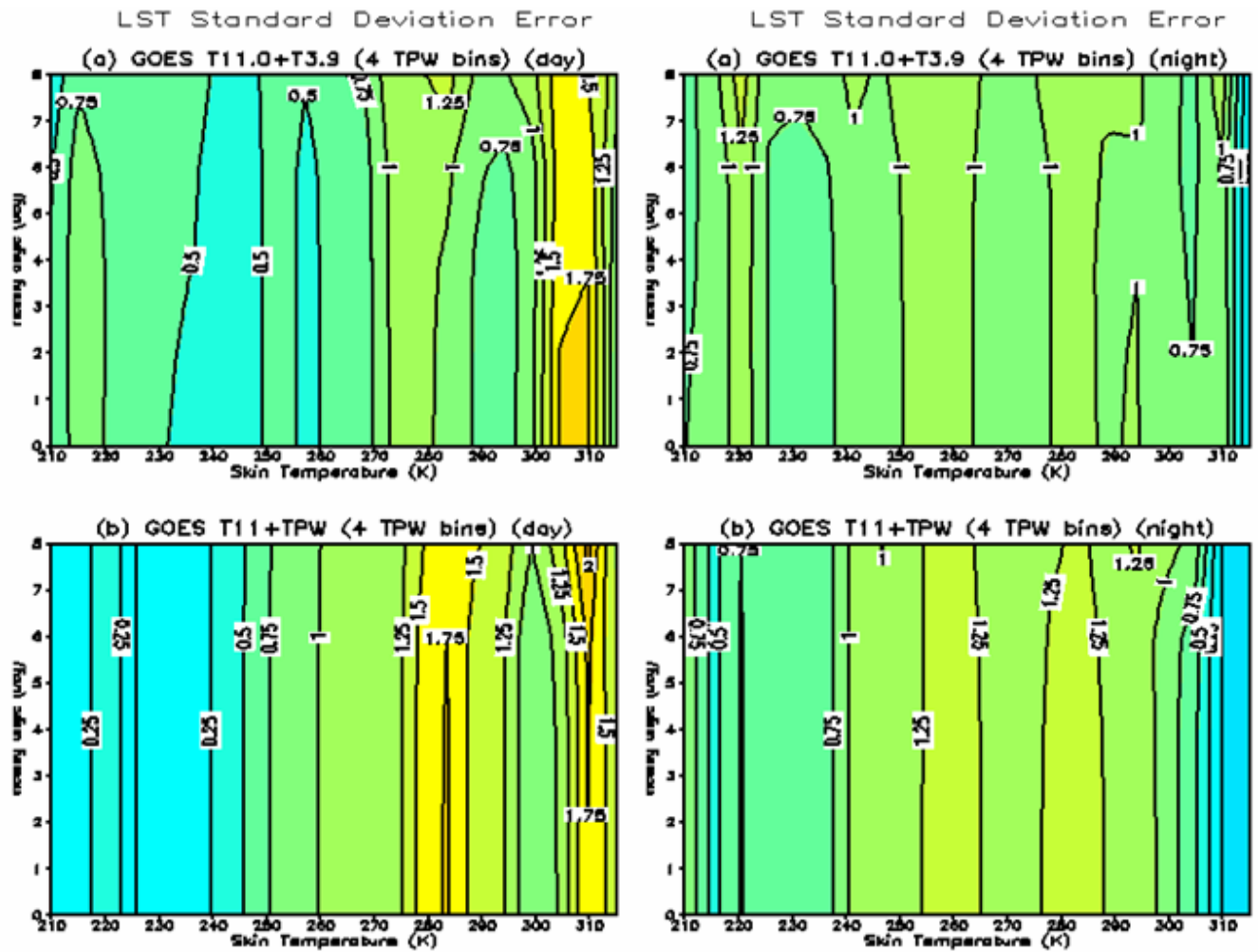
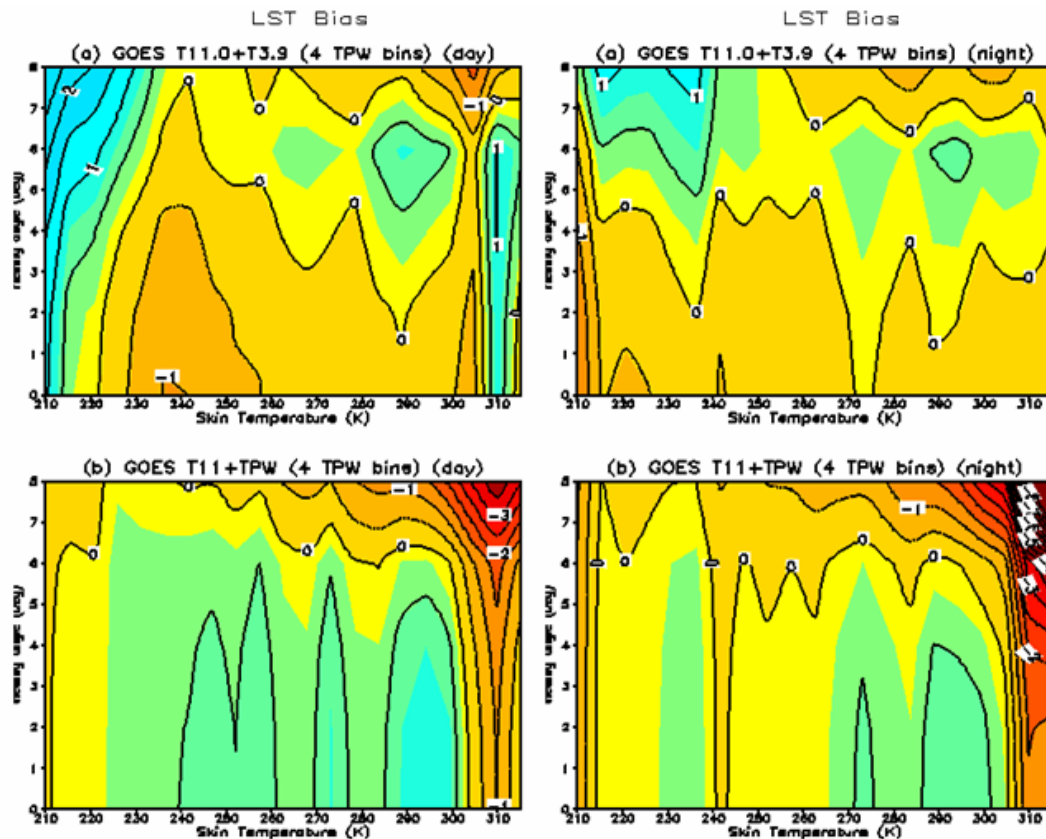


Figure 3.12. Standard deviation (STD) with water vapor bins are given for daytime (left) and nighttime (right).



**Figure 3.13. Bias errors of the regression analysis with water vapor bins are given for daytime (left) and nighttime (right).**

If we stratify LST retrieval according to water vapor intervals of  $2.0 \text{ g/cm}^2$ , then both standard deviation and bias errors show improvements than those without water vapor stratification. But one-channel algorithm still shows worse performance than dual-window algorithm.

Therefore, the dual-window algorithm is selected as the candidate LST algorithm for generating LST product from GOES 12-Q series.

For GOES imagers before GOES-12, to select the best algorithm for possible LST reprocessing, the comparison is conducted among the 9 split-window type algorithms and their modified forms, the following algorithms gave better performance than other split window algorithms:

- 1) The modified Becker and Li (1990) algorithm, which was a local split window algorithm, and later modified by Wan and Dozier (1996) to make the coefficients

varying with different conditions as the generalized split window algorithm. The maximum standard deviation is only 0.75 K for this algorithm.

- 2) The modified Sobrino 1993 algorithm (Sobrino 1993, Yu et al., 2007). The maximum standard deviation is only 0.75 K for this algorithm.

Meanwhile, it is found that the modified Sobrino (1993) algorithm with nonlinear term gave better performance than the modified Sobrino (1994) algorithm without nonlinear term. Nevertheless, Yu et al. (2007) found that the modified Ulivieri-1985 algorithm showed the least sensitivity to the emissivity variation, so they suggest this algorithm as the baseline GOES-R LST algorithm (Yu et al., 2010). In order to keep the consistency of LST product from different GOES platforms, we will also select this algorithm for possible LST reprocessing from GOES imagers before GOES-12.

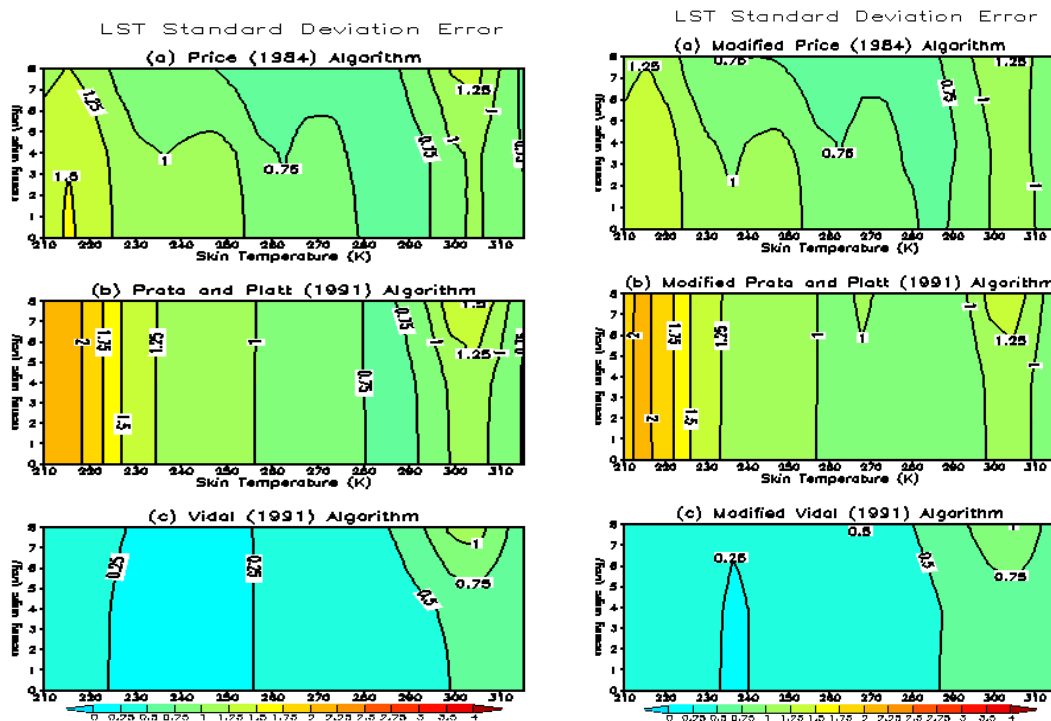


Figure 3.14. The standard deviation errors of LST retrieval from the forward GOES simulations for the 9 inherited SW algorithms and their modified forms.

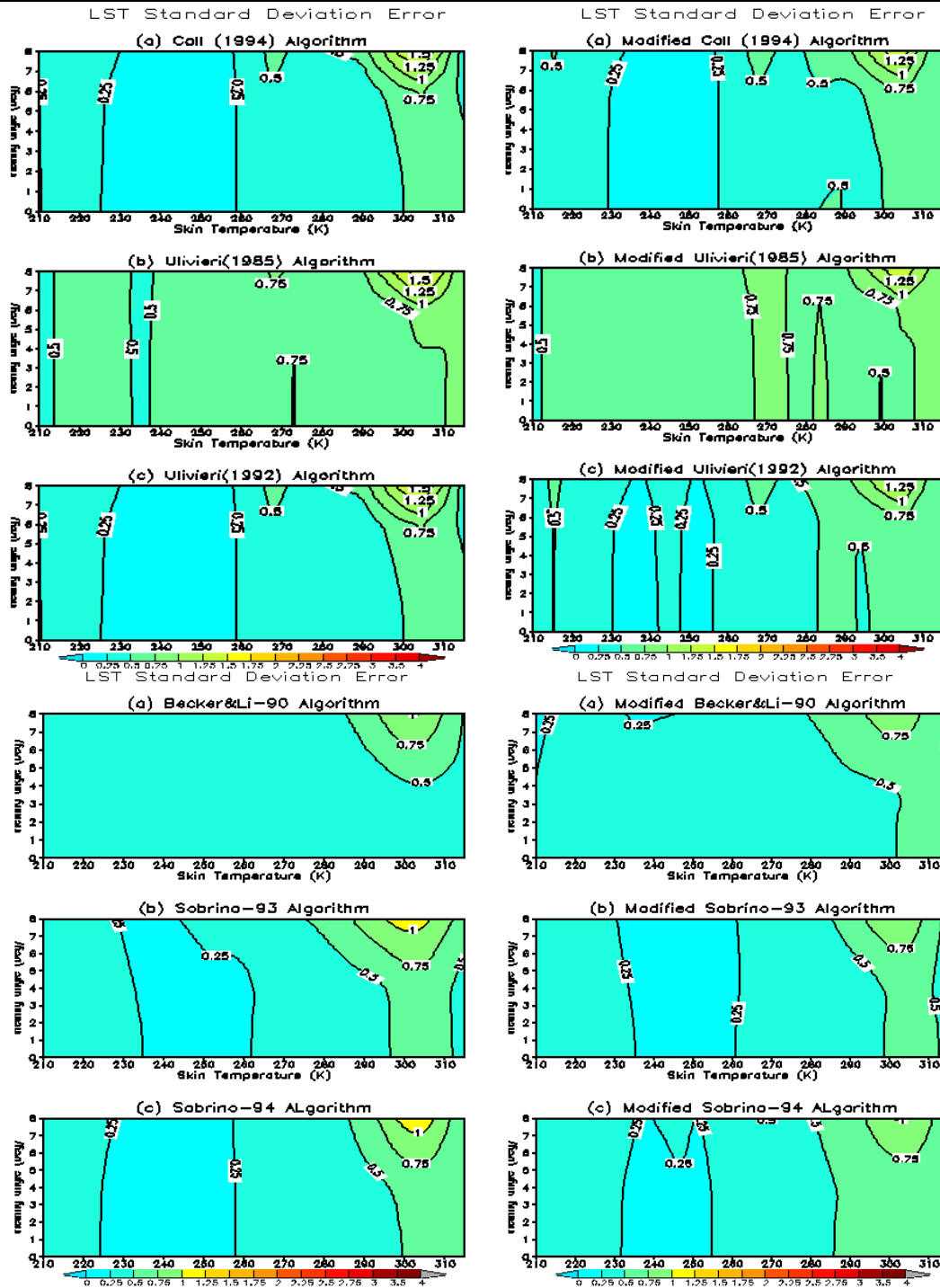


Figure 3.15. The standard deviation errors of LST retrieval from the forward GOES simulations for the 9 inherited SW algorithms and their modified forms.

### 3.3.3.4 Error Estimation

The GOES sensor view geometry may have significant impact on the variation of atmospheric absorption due to the radiative transfer path length increase from nadir to the edge of the scan. Considering that altitude of GOES satellite is about 36,000 km and the Earth radius is about 6700 km, the relationship between the satellite zenith angle ( $\theta$ ) and the satellite viewing angle ( $\theta_v$ ) is (Sun and Pinker, 2004)

$$\begin{aligned}\sin \theta &= \frac{\text{Satellite Altitude} + \text{Earth Radius}}{\text{Earth Radius}} \sin \theta_v \\ &\approx 6.37 \sin \theta_v\end{aligned}\tag{3.34}$$

Therefore, the maximum satellite viewing angle (about 8.7 degrees) corresponds to 74.48 degrees of view zenith angle. Such a large view zenith angle may have great impact on LST retrieval since, for instance, when the zenith angle is increased from 0 to 60 degrees, the atmospheric path length is doubled.

From Figures 3.8-3.13, we can see the algorithm STD and Bias error distributions with satellite zenith angle indicate, for the moist atmospheric conditions, the STD and Bias errors become significantly worse when the viewing zenith angle is larger than 6 or satellite zenith angle (SZA) larger than 42 degrees. For dry atmospheric conditions, the LST errors are less sensitive to viewing geometry

Two important error sources in LST retrieval are the surface emissivity uncertainty and the atmospheric water vapor absorption. We therefore analyzed the sensitivities of the candidate LST algorithms in terms of those two factors. The simulation dataset described above is used in the following estimations.

#### 3.3.3.4.1 Water Vapor Uncertainty

Figure 3.14 shows total column water vapor vs. LST distribution. As can be seen, most water vapor is concentrated at the warmer temperature range of 280–305 K and can vary from 0.25 to 7 cm due to increased evaporation from warmer surfaces, except for rocks, sand, and desert areas. This is why bigger errors occurred at temperature above 280 K (Figures 3.8-3.13), especially Bias error, show significant underestimate at warmer temperature. Furthermore, for the LST larger than 280 K with moist atmospheric conditions, such water vapor sensitivity increases when the satellite zenith angle increases. This is because the atmosphere is getting moister when the total column water vapor along the view path

increases with the increase of satellite zenith angle. For the lower LST cases (LST less than 280 K) with dry atmospheric conditions, the STD and Bias errors are not significantly sensitive to the view zenith angle.

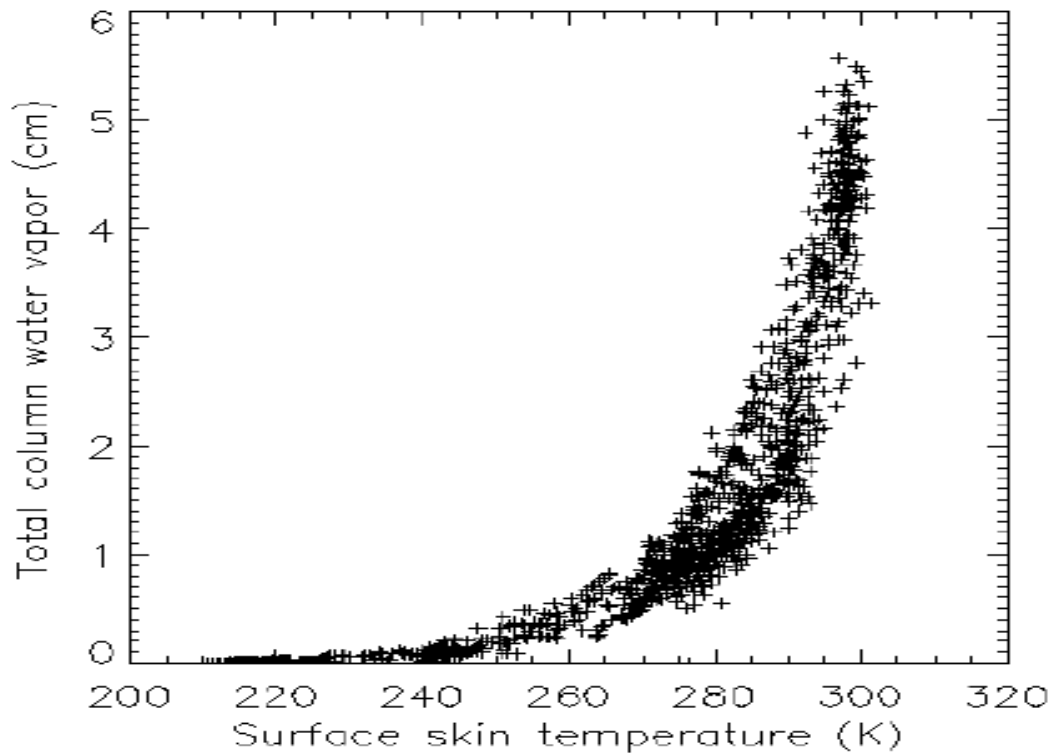


**Figure 3.16. Distributions of total column water vs. surface skin temperatures of the atmospheric profiles used in the simulation analyses (from Sun and Pinker, 2003)**

Stratifying our regressions by water vapor regime, we assume that water vapor content can be well estimated as *a priori*. In practice, water vapor information is usually available from satellite soundings, in-situ radiosondes and/or operational numerical weather prediction model forecasts. Nevertheless, two errors may occur. First, the water vapor value may be mis-measured due to a variety of error sources. Second, due to spatial resolution differences between the GOES observations and water vapor data, both “dry” and “moist” atmospheric conditions may occur within the unit spatial area over which the water vapor was estimated. For GOES LST product, we chose to use water vapor data from the GSIP data with 12.5 km spatial resolution, and one GSIP grid may contain three to more GOES pixels. Therefore, the coefficient set of the LST algorithm for dry atmospheres may be incorrectly applied in a moist atmospheric condition, and vice-versa.

### 3.3.3.4.2 Emissivity Uncertainty

An emissivity error can cause errors in the simulated brightness temperature and therefore an LST retrieval error. As shown in Figure 3.15, the brightness temperature error increases with the increase in emissivity error and is larger in the split-window channels at 11.0 and 12.0  $\mu\text{m}$  and smaller in the middle-infrared (MIR) 3.9  $\mu\text{m}$  band. The brightness temperature error due to emissivity error in Figure 3.15 is the average of all global data points over the entire temperature range. For a specific temperature the error may be larger.

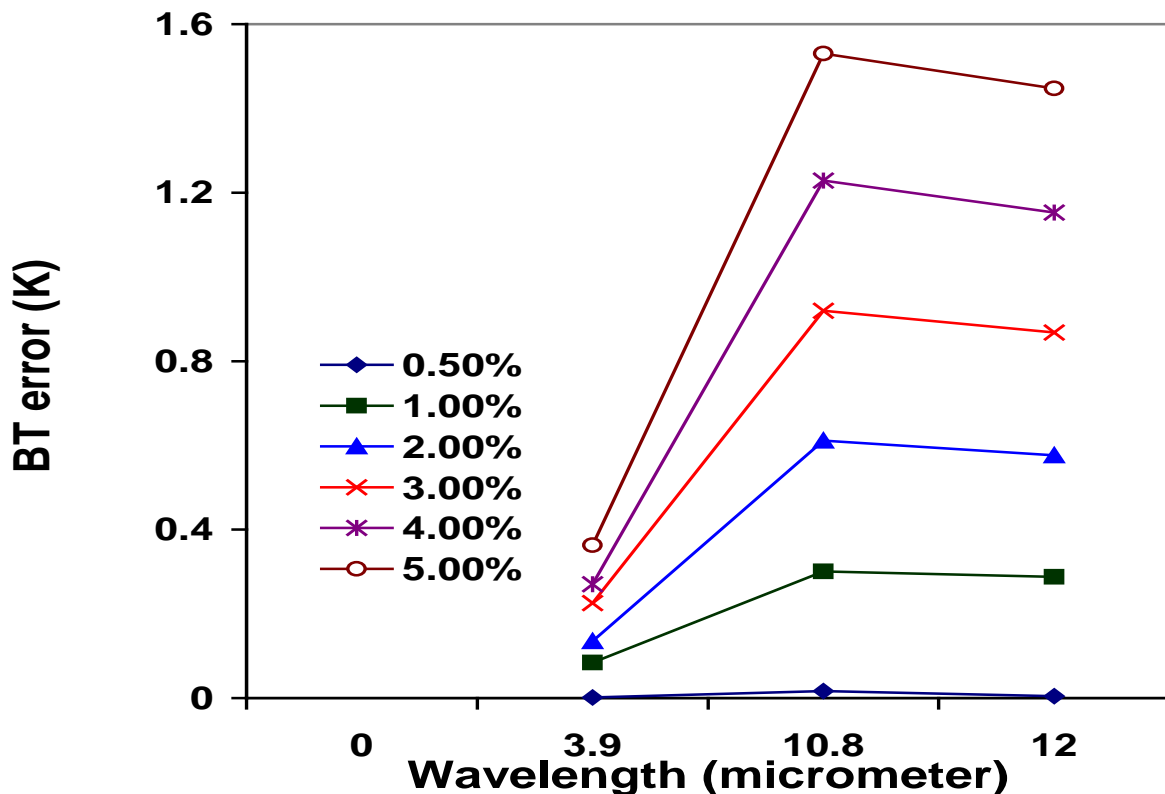


Figure 3.17. Distributions of brightness temperature (BT) errors due to errors in surface emissivity from the GOES forward simulations

As shown in Figure 3.16, emissivity variations are fairly small in the thermal IR bands (11.0 and 12.0  $\mu\text{m}$ ), but somewhat larger in the MIR band (3.9  $\mu\text{m}$ ); namely, an emissivity error causes a smaller brightness temperature error in the MIR band than in the thermal IR bands. This is another reason for us to introduce the dual-window algorithm.

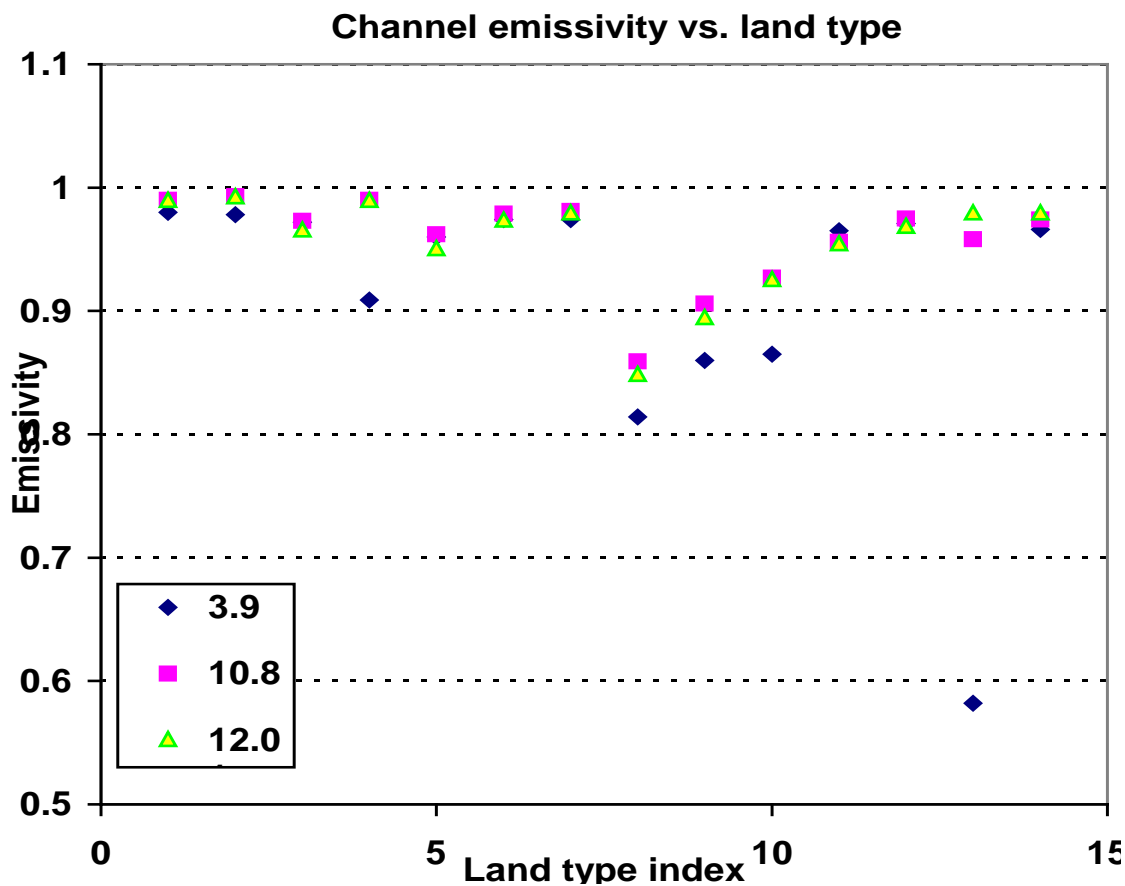


Figure 3.18. Spectral variation in surface emissivity for different surface types (from MOSART).

Analytically, the maximum LST uncertainty  $\delta T_s$  due to the emissivity uncertainty can be described as,

$$\delta T_s = \sqrt{\delta T_1^2 + \delta T_2^2} \quad (3.35)$$

where  $\delta T_1$  and  $\delta T_2$  represent the 3.9 and 11 micron band uncertainties resulting from the uncertainties of the mean emissivity ( $\varepsilon$ ) and emissivity difference ( $\Delta\varepsilon$ ), respectively. Using the Sobrino *et al.* (1994) split window algorithm as an example, these two components are

$$\delta T_1 = (A_3 - \frac{A_4}{\varepsilon^2})\delta\varepsilon \quad \text{and} \quad \delta T_2 = \frac{A_4}{\varepsilon} \delta(\Delta\varepsilon) \quad (3.36)$$

Therefore, the maximum LST uncertainty is

$$\delta T_s = \sqrt{((A_3 - \frac{A_4}{\varepsilon^2})\delta\varepsilon)^2 + (\frac{A_4}{\varepsilon} \delta(\Delta\varepsilon))^2} \quad (3.37)$$

From the above equations, we can see, to reduce the LST algorithm sensitivity to the emissivity error, the emissivity difference should not be included in the algorithm formulation. Moreover, simplicity is an advantage in operational procedures, so the Ulivieri and Cannizzaro (1985) split window algorithm was chosen as the baseline GOES-R LST algorithm (Yu *et al.*, 2011), to be consistent with GOES-R LST product, this algorithm is also selected as the baseline algorithm for historic LST retrieval from GOES 8-11.

### 3.3.3.5 Summary of Algorithm Selection

The accuracy difference between the moist and dry atmospheric conditions implies that water vapor contamination is a major concern for the GOES-imager LST retrieval. The largest errors are expected with SW algorithms when the atmosphere is moist and the satellite zenith angle is larger than 45 degrees. Accuracy of the retrieval under dry atmospheric conditions is significantly better than that under moist atmospheric conditions. Similar results were observed in Yu *et al.* (2008).

Emissivity sensitivity is a more serious problem. This is because the emissivity effect is coupled with the atmospheric absorption effect in the radiative transfer process; while the atmospheric absorption effect is linearized in the SW technique, the emissivity effect cannot be similarly linearized. A trade-off in current SW applications occurs since emissivity information improves retrieval accuracy, but inaccurate emissivity information may induce significant error. It is worth pointing out that the same conflict also occurs in all the SW LST algorithms, e.g., the LST algorithm developed for the NPP VIIRS sensors (Sikorski *et al.*,

---

2002), that stratify the algorithm coefficients for different land surface types instead of using the emissivity information explicitly in the algorithm. For such algorithms, the emissivity uncertainty of a certain surface type may also induce significant LST retrieval error.

Our results demonstrate that, although algorithms using both the mean emissivity and the emissivity difference of the two thermal channels, such as the modified Becker and Li (1990) algorithm, provide the best retrieval accuracy, such algorithms are too sensitive to the emissivity uncertainty and should not be used in operational practice. As a compromise, we recommend modified Uliveri (1985) algorithm, which only requires the mean emissivity information, as the baseline algorithm for LST retrieval for GOES imagers with split-window channels for generating the GOES-imager LST product, to be consistent with GOES-R LST algorithm too (Yu et al., 2010). For LTS retrieval from GOES M (12)-Q series, we recommend using dual window algorithm.

Finally, we emphasize that all the results discussed to this point assume perfect cloud detection. That is, all these results are for truly cloud clear pixels. Residual cloud effects in pixels detected as clear will add significant noise to the LST retrievals.

### 3.4 Algorithm Output

Output of the LST algorithm mainly contains two data arrays: the LST values and associated quality control flags, which are described in Tables 3.5 and 3.6.

**Table 3.5. Algorithm output data.**

Name	Type	Data type	Description
LST values	Output	16-bit Int(scaled) In NetCDF format	Retrieved land surface temperature value for each pixel of the scanning mode in NetCDF format
LST values	Output	16-bit Int (scaled) In GRIB2 format	Retrieved land surface temperature value for each pixel of the scanning mode in GRIB2 format
LST values	Output	Byte(scaled) In JPEG format	Retrieved land surface temperature value for each pixel of the scanning mode in JPEG file
Quality Control flags	Output	Byte	Quality control flags for each pixel of the scanning mode: Land, cloudiness, sensor data quality, day/night, very moist, large view zenith, very cold surface, etc.
Image Date	Output	Int	Image date

# NOAA NESDIS STAR

## ALGORITHM THEORETICAL BASIS DOCUMENT

Version: 1.0

Date: January 17, 2012

TITLE: GOES LST Algorithm Theoretical Basis Document

Page 58 of 81

Image Time	Output	Int	Image time
Longitude	Output	Float	Pixel longitude
Latitude	Output	Float	Pixel Latitude

In addition, the LST retrieval processing will also produce some metadata describing processing information (e.g. date/time stamps), as well as inherit some metadata from the sensor input data.

Specifically, the common metadata providing general information about the product includes product name, satellite identification, instrument identification, projection, product resolution (at nadir), date and time, bounding box, byte order information, product version number, data format/compression type, ancillary data to produce product (including product precedence and interval between datasets is applicable), production location and contact information. Moreover, metadata provides additional LST specific statistics such as minimum/maximum/SD of LST retrievals, total numbers of good LST retrievals, abnormal retrievals *et al.*

**Table 3.6. Quality control flags at pixel level.**

Byte	Bit	Flag	Source	Effect
1	0-1	Empty		Reserved for future use
	2-3	GSIP Data Availability	GSIP	00=normal, 01=bad data, 10=missing data
	4-5	Surface Type	Land type	00 = land, 01 = not land, 10=out of space
	6-7	Cloud	Cloud Mask (GSIP L2)	00=clear, 01=probably clear, 10=probably cloudy, 11=cloudy
2	0-1	Snow	Snow fraction (GSIP L3)	00=snow free (mean snow fraction < 0.2), 01=snow contamination (mean snow fraction >=0.2), 10=filled value
	2	Day/Night	Solar zenith (GSIP L1)	0=day (solar zenith <= 85 deg), 1=night
	3	View Angle	Sensor zenith (GSIP L1)	0=normal, 1=large view angle (LZA>55 deg)

# NOAA NESDIS STAR

ALGORITHM THEORETICAL BASIS DOCUMENT

Version: 1.0

Date: January 17, 2012

TITLE: GOES LST Algorithm Theoretical Basis Document

Page 59 of 81

	4-5	Atmospheric Condition	Mean TPW (GSIP L3)	00=dry atmosphere ( $wv \leq 2.0g/cm^2$ ); 01=moist atmosphere( $wv > 2.0g/cm^2$ ); 10= very moist( $wv > 5.0/cm^2$ ), 11=filled value
	6-7	LST Quality	LST	00=normal (250 - 330K), 01= out of range, 10=cold surface (LST retrievals $< 250 K$ & $\geq 210K$ ), 11=filled value

Note: monitoring process should only use byte 1 values for the monitoring purpose (0 indicates good, otherwise bad).

## 3.5 Performance Estimates

### 3.5.1 Test Data

The performance of the selected algorithm must be verified using real satellite data, and be validated using ground measurement. The imagers of U.S. GOES series 12 and 13 are tested. Table 3.5 lists the sensor spectral specifications of the GOES-12/13 imagers ([http://rammb.cira.colostate.edu/projects/goes-o/NOAA Tech Report NESDIS 131 GOE S-14 Science Test.pdf](http://rammb.cira.colostate.edu/projects/goes-o/NOAA_Tech_Report_NESDIS_131_GOE_S-14_Science_Test.pdf)).

**Table 3.7 Comparison of GOES-12 and GOES-13 imager channels**

Sensor	Channel No.	Wavelength Center ( $\mu m$ )	Bandwidth ( $\mu m$ )	Sensor Noise ( $NE\Delta T$ K)
GOES-12	2	3.9	3.8 ~ 4.0	0.13@300K
	4	10.7	10.2 ~ 11.2	0.11@300K
GOES-13	2	3.9	3.8 ~ 4.0	0.051@300K
	4	10.7	10.2 ~ 11.2	0.053@300K

It is worth noting that algorithm coefficients applied for different sensor inputs are different although the algorithm bears the same formulation throughout all the tests described in this section. This is because the central wavelengths and spectral response functions of the window channels are slightly different from different GOES imager window channels. To calculate the algorithm coefficients applicable to different GOES imager inputs, we used the same simulation dataset and regression procedure (Section 3.3.3), but used the

corresponding central wavelengths and spectral response functions of the window channels in the simulation model.

To evaluate the selected GOES-imager LST algorithms, we collected ground reference LST data estimated from the observations of six SURFRAD stations, and compared the satellite retrieved LST values. The sensor inputs of the algorithm are from the GOES-12 imager observations.

### **3.5.1.1 GOES-imager Data**

The GOES-12 imager dataset were obtained from the National Climate Data Center (NCDC) via the CLASS web interface. It is 4-km in spatial resolution and 1-hour in temporal resolution. In this validation effort, we selected the imager pixels that were spatially nearest to the SURFRAD locations. Available in this dataset are the hourly brightness temperature measurements from the five channels of GOES-12 and the associated illumination and viewing geometry. The thermal infrared channels of GOES-12 imager are listed in Table 3.7. Figure 3.17 shows some examples of LSTs derived from the real GOES-12 measurements.

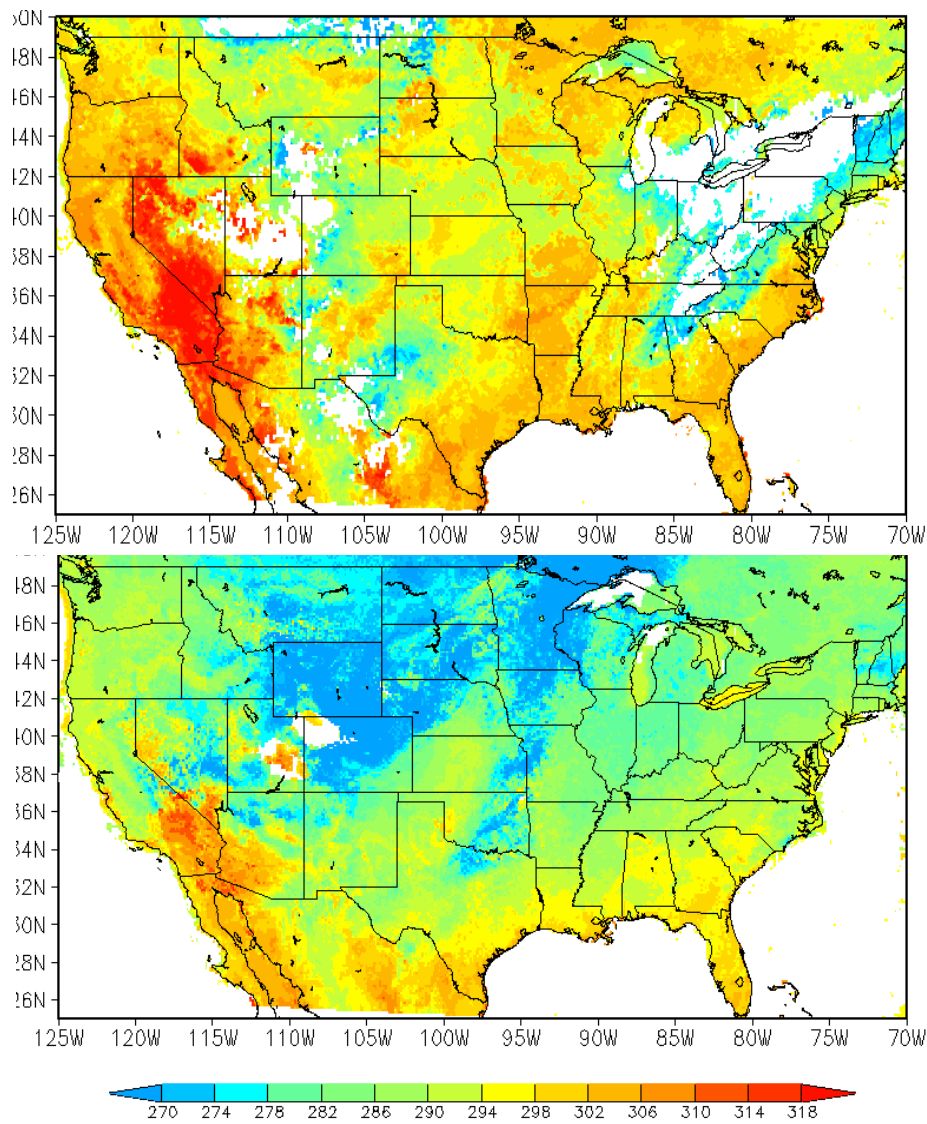


**Figure 3.19. LST derived from the GOES-12 observations on 07/31/2004 (upper) and 10/01/2004 (lower).**

### 3.5.1.2 Ground Truth Data

The Surface Radiation Budget Network (SURFRAD) network has been operational in the United States since 1995. It provides high quality *in situ* measurements of upwelling and downwelling longwave radiations, along with other meteorological parameters such the atmospheric water vapor. A detailed description of the SURFRAD network and associated instrumentation can be found in Augustine *et al.* (2000; 2005). Table 3.6 gives brief information about the six SURFRAD stations related to this work.

We used one year (2010) of SURFRAD data over the six stations to validate the performance of a set of seasonal regression models.

**Table 3.8 SURFRAD Stations used for the algorithm validation.**

Site No.	Site Location	Lat(N)/Lon(W)	IGBP Surface Type
1	Bondville, IL	40.05/88.37	Crop Land
2	Fort Peck, MT	48.31/105.10	Grass Land
3	Goodwin Creek, MS	34.25/89.87	Deciduous Forest
4	Table Mountain, CO	40.13/105.24	Crop Land
5	Desert Rock, NV	36.63/116.02	Open Shrub Land
6	Pennsylvania State University, PA	40.72/77.93	Mixed Forest

Surface type information for the sites was obtained from the University of Maryland (UMD) land classification dataset (Hansen and Reed, 2000; Pinker et al., 2009). In the time domain, we used only the SURFRAD values that were closest to the GOES-12 measurements. The maximum temporal difference between the SURFRAD and the satellite measurements was less than 2 minutes since the SURFRAD daily files provide measurements every 3 minutes. A whole year of 2004 was used in this comparative analysis.

The SURFRAD ground LST values were calculated from upwelling and downwelling longwave radiation measurements, in the spectral range from 3  $\mu\text{m}$  to 50  $\mu\text{m}$ , obtained by a precise infrared radiometer (PIR). The SURFRAD PIR is calibrated annually using a laboratory blackbody such that its measurement estimates the total energy emitted from a blackbody rather than the instrument limited spectrum (Augustine *et al.*, 2000; 2005). The surface skin temperature,  $T_s$ , can be estimated using

$$T_s = (R^\uparrow - (1-\epsilon)R^\downarrow) / (\sigma\epsilon)^{1/4} \quad (3.38)$$

where  $R^{\uparrow}$  and  $R^{\downarrow}$  are the upwelling and downwelling longwave fluxes, respectively,  $\varepsilon$  is the surface emissivity, and  $\sigma$  is the Stefan-Boltzmann constant, which has a value of  $5.67051 \times 10^{-8} \text{ Wm}^{-2}\text{K}^{-4}$ .

The surface broadband emissivity in equation (3.37) was estimated from MODIS spectral emissivity using narrowband to broadband conversion method (Wan and Li, 1997; Jin and Liang, 2007). The mapping method is described in (Yu *et al.*, 2005; Pinker *et al.*, 2009).

### 3.5.1.2 Match-ups

To get pairs of valid match-up LSTs from the GOES-imager and SURFRAD data, we take three general steps:

- 1) geo-location match-up
- 2) time match-up
- 3) cloud screening for clear-sky cases.

We first pick up the GOES imager pixel that is spatially nearest to one of the SURFRAD locations, and then search the SURFRAD time segment that is closest to the imager data time stamp in the time series of the matched SURFRAD station. The geo-location match-up accuracy is limited by the accuracy of GOES-imager data, which is about 4 km; while the time match-up accuracy is basically determined by imager scanning time and temporal interval of the SURFRAD measurement, which is approximately about 5 minutes.

Once the valid match-up are confirmed, LSTs of that specific location and time are calculated separately from the GOES-imager data and the SURFRAD data. If a cloudless data pair is further confirmed following the cloud screening scheme, the matched LST pair is archived together with other relevant ancillary data.

## 3.5.2 Test with GOES-12 Observations

### 3.5.2.1 Comparison of Dual Window and Split Window Algorithms

It is appropriate here to examine whether the LST retrieved from the dual-window ( $3.9 \mu\text{m} + 11 \mu\text{m}$ ) algorithm is comparable to LST derived from the split-window algorithm that has never been compared before, to ensure the applicability of the dual-window algorithm in the future. For each of the two algorithms, we calculated the Bias, standard deviation (STD) and

Root Mean Square (RMS) errors in the satellite LST retrieval as evaluated against the in-situ observations (Figure 3.18).

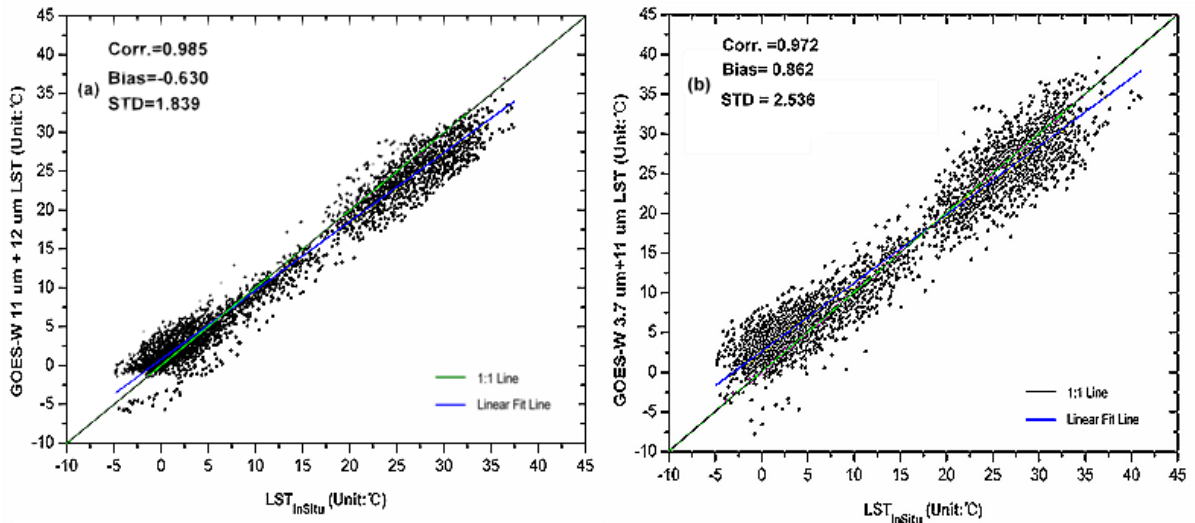


**Figure 3.20. Scatter plots of LST derived from the GOES vs. in-situ observations for: (a) split-window algorithm, and (b) dual-window algorithm.**

The scatter plots shown in Figure 3.18 indicate that both algorithms perform well, since they have fairly good correlation with the ground-observations, though the scatter distribution of the dual-window (3.9  $\mu\text{m}$  + 11  $\mu\text{m}$ ) algorithm is worse than the split-window (11  $\mu\text{m}$  + 12  $\mu\text{m}$ ) algorithm, bringing about the STD error of 2.53 K from the dual-window algorithm, as compared to 1.83 K from the split window algorithm.

However, in general, all of accuracy comparisons show that using the dual-window to derive LST is fairly feasible, though its total accuracy is slightly worse than those from the split-window algorithm. These results show that the lack of split-window channels on the GOES M-Q series may degrade the performance of GOES LST retrieval.

### 3.5.2.2 Comparison of LSTs from GOES and MODIS

In the previous ATBD version (2.0), we compared LST retrievals from the GOES sensors with those from polar orbiting sensors, such as the MODIS. These comparisons were made to provide a preliminary indication of GOES algorithm performance. Since then, more comprehensive testing has been performed. These test results, described in Section 3.5.2.4, provide a better indication of performance, so the GOES MODIS comparisons have been removed from this ATBD version.

### 3.5.2.3 Precision and Accuracy Estimates

Table 3.9 shows the evaluation results of the GOES-12 LST from the dual-window algorithm with emissivity approach against the SURFRAD observations at the six stations. The accuracy (ACC) represents the mean bias (difference) error between GOES-LST and SURFRAD observations. The precision (PREC) represents the standard deviation error between GOES-LST and SURFRAD observations. N indicates the total sample numbers. The station ID (STAID) is:

STAID=1, Bondville, IL

STAID=2, Fort Peck, MT

STAID=3, Goodwin Creek, MS

STAID=4, Table Mountain, CO

STAID=5, Desert Rock, NV

STAID=6, Penn State, PA

Shown in Table 3.9 are the accuracy/precision values for the four seasons, respectively. It is worth of noting that the seasonal precision values are still around 2.5K. But the seasonal accuracy patterns vary from site to site. It is unsure whether such distinct seasonal patterns might be related to the different surface covers and regional climates. All these statistical features will be further studied in the future.

**Table 3.9 Seasonal Accuracy/Precision Estimations from GOES-12 LST Retrieval**

Site	January			April			July			October		
	N	ACC	PREC	N	ACC	PREC	N	ACC	PREC	N	ACC	PREC
1	164	-1.64	1.46	120	-1.83	1.93	151	-2.18	1.49	121	-0.32	1.75
2	188	-1.27	2.28	71	-2.88	1.54	146	-2.94	1.48	74	-0.38	2.57
3	208	-1.13	1.64	183	-1.53	1.89	104	-2.89	1.43	163	0.12	1.81
4	206	-0.53	2.15	145	-0.02	2.28	209	0.11	1.95	192	-1.01	1.85
5	182	-1.33	2.00	127	-1.42	2.49	167	-1.41	2.08	135	-0.13	2.65
6	133	-1.68	2.34	99	-1.46	2.23	169	-1.08	2.30	133	1.56	2.65

---

Big errors are found in winter, especially over the cold surface where surface temperatures are below freezing point or less than 273 K or 0° C. We therefore doubt if it is because of snow contamination. We therefore separate surface into snow and snow-free cases, as shown in Table 3.10.

**Table 3.10 Statistics of LST retrieval accuracy and Precision**

Date	Time	Ground Temperature	Sample size	Correlation coefficient	Accuracy	Precision
0401	Daytime	Surfrad	98	0.9554	1.6401	2.3280
0401	Nighttime	Surfrad	798	0.8614	2.8162	3.0006
0401	Daytime-snowfree	Surfrad	70	0.9448	1.7335	2.2032
0401	Nighttime snowfree	Surfrad	696	0.8614	2.5822	3.0233
0401	Daytime-snow	Surfrad	13	0.9534	1.4844	0.8024
0401	Nighttime-snow	Surfrad	32	0.9356	1.4157	0.8750

However, it is found that snow-free cases don't show improvements to the precision, for the pixels with snow cover less than 5%, there are still many pixels with extremely low observed brightness temperature, which can be different from the SURFRAD measurements as big as 28 degrees. Details are shown in Table 3.11.

**Table 3.11. Records with big errors from NCDC data (Cloud free & snow free)**

$T_{11}$	Retrieved temperature (LST)	Surfrad ( $T_s$ )	Differences ( $T_s - T_{11}$ )	Differences ( $T_s - LST$ )	Snow cover	Cloud cover
244.983	252.481	273.544	28.561	21.063	0	0
259.486	262.779	284.125	24.639	21.347	0	0
253.324	257.159	274.78	21.457	17.621	0	0
253.211	258.288	273.93	20.719	15.642	0	0
250.29	255.969	270.233	19.942	14.264	0	0
255.457	259.804	275.249	19.791	15.445	0	0
261.585	263.889	281.067	19.482	17.178	0	0
266.798	269.673	285.263	18.465	15.59	0	0
261.753	265.402	280.157	18.404	14.755	0	0
251.984	258.238	269.789	17.806	11.551	0	0
246.885	252.160	264.610	17.725	12.450	0	0
259.854	264.458	277.126	17.272	12.669	0	0
257.4	269.883	274.586	17.185	4.702	0	0
263.07	265.670	280.136	17.067	14.466	0	0
267.701	269.405	284.760	17.060	15.355	0	0
267.566	288.035	284.273	16.707	3.762	0	0

Big retrieval errors are caused by these pixels with extremely low temperature. We therefore analyzed temperatures of cloud and snow cover pixels. For cloudy pixels, as shown in Table 3.12, the average temperatures of GOES  $T_{11}$  and ground observations for all the pixels with cloud cover possibility larger than 90% are computed, which are 252.27 and 270.55, respectively. The average difference can reach as large as 18 degrees. While for snow pixels with snow cover larger than 5% (Table 3.13), average brightness temperature at 11  $\mu\text{m}$  is not that different from the ground measurements. The mean difference is less than 5 degrees. From this analysis, we think the big differences are more probably not caused by snow, but rather by cloud contamination, which the cloud cover algorithm may fail to detect. If all these contaminative pixels with the  $T_{11}$  less than the average cloud top temperature, then the results show improvements (Table 3.14).

**Table 3.12. Statistics of cloud cover pixels**

Cloud	GOES T <sub>11</sub> (K)	Surfrad (K)	Differences (K)
Max	285.7590	296.6778	68.9041
Min	214.5910	236.1000	0.0062
average	252.2728	270.5534	<b>18.40956</b>

**Table 3.13 Statistics of snow cover pixels**

Snow	GOES T <sub>11</sub> (K)	Surfrad (K)	Differences (K)
Max	265.2350	268.9851	27.4411
Min	223.9190	247.2088	0.0141
average	254.2187	258.9029	<b>4.919885</b>

**Table 3.14 Statistics of LST retrieval accuracy after removing possible cloud contamination**

Date	Time	Ground Temperature	Sample size	Correlation coefficient	Bias error	Precision error
0401	daytime	Surfrad	96	0.9829	1.1725	1.3324
0401	Nighttime	Surfrad	752	0.9408	1.9687	1.8893
0401	Daytime snowfree	Surfrad	68	0.9797	1.0963	1.3307
0401	Nighttime snowfree	Surfrad	654	0.9422	1.8102	1.8706
0401	Daytime-snow	Surfrad	13	0.9534	1.4844	0.8024
0401	Nighttime-snow	Surfrad	32	0.9356	1.4157	0.8750

### 3.5.2.4 Performance Estimates from GOES LST system test

GOES LST system generates a series of GOES LST products for a consecutive 30 days. GSIP products from Oct. 2011 have been downloaded to test the GOES LST software at system level. GSIP products can be acquired from <ftp://ftp.orbit.nesdis.noaa.gov/pub/smcd/gsip/experimental/GENHEM/>.

One month (Oct. 2011) of SURFRAD data over six stations have been used to validate the accuracy of GOES LST products. SURFRAD data can be acquired from Earth System Research Laboratory, NOAA. <ftp://ftp.srrb.noaa.gov/pub/data/surfrad/>.

Matched-up ancillary data including land/sea mask, emissivity data and lookup table for coefficient are also required in this system test item.

We have totally 316 match-up pairs of GOES LST and SURFRAD observations after removing those pixels that might be cloud contaminated. The precision for Oct. 2011 data is 2.17291 K and the accuracy is -0.78229K, which meet the requirement for accuracy and precision as 2.3 K and 2.3K, respectively. The scatter diagrams are shown in figure below.

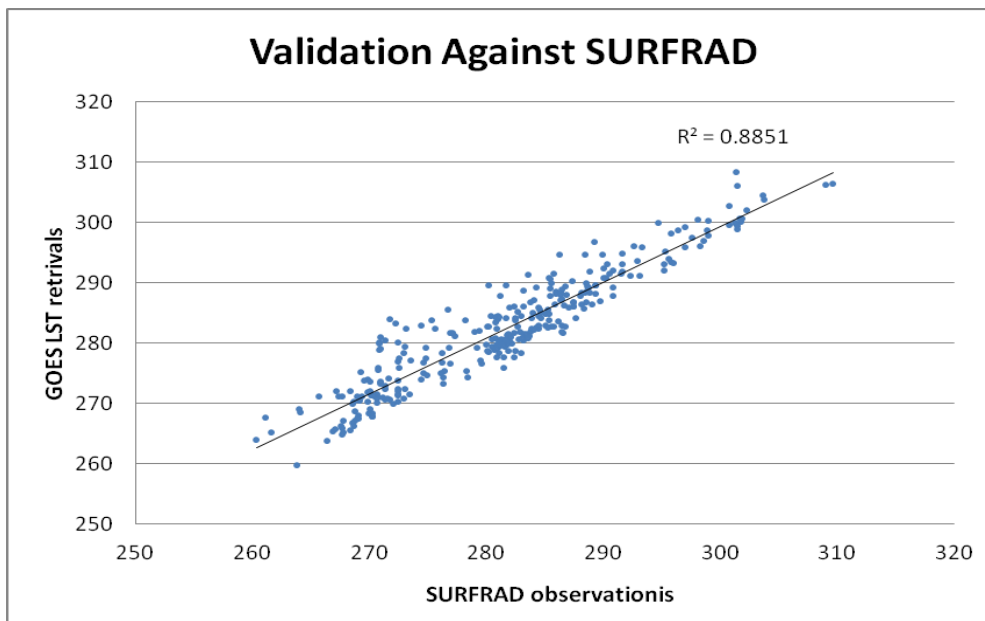


**Figure 3.21. Scatter plots of LST derived from GOES vs. SURFRAD observations**

### 3.5.3 Test with GOES-13 Observations

Dual window algorithm has been applied to current GOES-13 observations, which were obtained from the NCDC CLASS and from the GSIP source with matched L1/L2/L3 data provided by Dr. Istvan Laszlo and William Straka. ▶

#### 3.5.3.1 The impacts of emissivity on GOES LST product

Since it's impossible to obtain current month or weekly emissivity data for operational LST product generation, the only emissivity data available is the emissivity data from previous month or week; from the same month or week of last year, or from long-term mean historic emissivity database. MODIS monthly and weekly emissivity data were obtained from NASA.

The 12-month historic emissivity dataset was generated as long-term 10-year (2001-2010) average of monthly data. We have studied the impact of different emissivity on GOES LST product quality.

**Table 3.15. Emissivity dataset dependence of retrieval quality**

Date	Emissivity	Sample size	Accuracy	Precision
2010.12	Historical	711	1.6637	1.5380
	Previous month	711	1.6110	1.5499
	Current-month	711	1.6303	1.5627
	Same month in last year	711	1.6356	1.6611
	Weekly*	711	8.5269	41.4239
	Weekly**	683	1.6330	1.4989
2010.07	Historical	1534	1.1307	1.1125
	Previous month	1534	1.1770	1.1468
	Current-month	1534	1.1490	1.0973
	Same month in last year	1534	1.1388	1.1344
	weekly	1536	1.1504	1.0837

\* Weekly results include some unreasonable retrieved temperature due to a problematic emissivity data (in week3) at the station Penn State, PA, the emissivity value is 0.094 and 0.099 compared to the normal value of 0.952 and 0.975 in other weeks. There is no obviously abnormal emissivity found in July 2010.

\*\* The result for ruling out those unreasonable records with problematic emissivity.

The results show that LST retrieval errors are still larger in winter, especially, big errors are found for cold temperatures below 240 K, and may suggest cloud contamination problem may be more severe in winter time. It is found that the weekly emissivity may be unstable, unreasonable emissivity of 0.094 and 0.098 is found at the SUFRAD Penn State site. If the records with these unreasonable emissivity values are removed, then weekly emissivity data yield the best results with the errors as the lowest, followed by the current month emissivity. Historic emissivity data gave better results than previous month emissivity. The results show

that due to the possible instability in weekly emissivity data, and the unavailability of current month emissivity data at the operational time, using historic emissivity gave better LST retrievals than using previous month emissivity, so we suggest using historic emissivity data in operational LST product.

### 3.5.3.2 Comparison with the GSIP LST product

Comparison between GOES LST retrievals and GSIP LST Product has been made for April 18<sup>th</sup> 2010 (spring), June 3<sup>rd</sup> 2010 (summer), October 20<sup>th</sup> 2010 (fall), January 1<sup>st</sup> 2011 (winter). GOES LST derived from dual-window algorithm at pixel level is aggregated or re-sampled to the same spatial resolution as the GSIP L3 product (1/8 degree) and then the difference is compared. It is found in general, GOES LST is about 2 K higher than GSIP LST.

**Table 3.16. Difference between GOES LST and GSIP LST**

Date	Mean difference	Standard deviation
April 18 <sup>th</sup> 2010 (164519)	2.3172	2.4191
June 3 <sup>rd</sup> 2010 (164518)	2.3553	2.5796
Oct. 20 <sup>th</sup> 2010 (214519)	2.3930	3.1044
Jan. 1 <sup>st</sup> 2011 (004520)	2.0824	2.2987

We have also evaluated GOES-13 LST retrievals from dual-window algorithm with historic emissivity and GSIP LST product against the SURFRAD observations for four mid-season months in April, June, and October in 2010 and January 2011. GOES LST is derived from current GOES-13 observations, and compared with the GSIP L3 LST output. In general, GOES LST shows lower errors or better accuracy than the GSIP LST.

**Table 3.17. Comparison of GOES LST and GSIP LST against ground LST**

Date	Product	Sample size	Accuracy	Precision
2011.01	GSIP	729	2.7168	2.9180
2010.04	GSIP	466	3.1753	3.2730
2010.07	GSIP	1215	2.8393	2.4888
2010.10	GSIP	820	2.5645	2.4968
2011.01	GOES LST	974	1.6850	2.2935
2010.04	GOES LST	602	1.7140	1.3823
2010.07	GOES LST	1591	1.1660	1.1561
2010.10	GOES LST	1406	1.6730	2.3233

### 3.5.4 Error Budget

The test results shown in Section 3.5.2.3 indicate that overall the accuracy and precision of the selected algorithm meets requirements (2.3 K). Such assessment is based on the simulation dataset, and the GOES imager and SURFRAD ground measurement match-up dataset.

As mentioned earlier, there are several issues that should be further studied in the match-up dataset comparisons. Particularly, difference between the satellite pixel-size measurement and the ground spot-size measurement must be characterized for a high quality validation procedure.

Accuracy of the SURFRAD LST estimation is also a concern since it is calculated from the upwelling and downwelling irradiance with a broadband surface emissivity value. The emissivity values is estimated from the surface type classification and the emissivity mapping (Snyder et al, 1998) or converted from MODIS spectral emissivity, which may be problematic and introduce the ground LST estimation error.

Cloud contamination is still a problem even if we have used a stringent cloud filtering procedure in generating the match-up dataset. It is found that a little threshold value or procedure change will have significant impact to the output match-up data pairs, though the overall validation results are not obviously affected.

Errors will also be introduced in the algorithm coefficients generation using the MODTRAN radiative transfer model. This is mainly because limited samples of the atmospheric profiles, solar-view geometries, surface emissivity values and the prescribed surface temperatures were used in the simulation process. Also, the simulated sensor response function used in generating the sensor brightness temperature maybe an error source.

All the above factors may potentially degrade the algorithm performance when it is applied to the real GOES-M (12)-Q satellite observation.

### 3.6 Practical Considerations

#### 3.6.1 Numerical Computation Considerations

The LST algorithm selected is mathematically simple, and requires no complicated mathematical routines. In operations it will be robust and fast enough in terms of the

algorithm latency requirement (< 30 minutes) using current computer power. There is no specific numerical computation requirement needed. For storage consideration, LST values should be saved in two-byte integers, with scale factors (intercept and slope) defined for the entire dataset. Quality flags for each pixel value should be bit-flag definitions, to minimize data storage.

### **3.6.2 Programming and Procedural Considerations**

The LST algorithm is a pixel-by-pixel algorithm, implemented in sequential mode. Because of the algorithm simplicity, it requires small amount of code, with basic mathematical routines. However, since the LST algorithm requires ancillary datasets such as emissivity data and the total column atmospheric water vapor data, pre-calculated lookup tables may be needed for mapping the ancillary datasets to the GOES Imager pixel geolocation. Besides, the algorithm preprocessing routines for calibration and geolocation should be programmed in block functions for integration ease.

#### **3.6.2.1 Configuration of Retrieval**

The primary adjustable parameters for the LST retrieval are the algorithm coefficients that are stratified for different atmospheric conditions according to the atmospheric column water vapor with 2 g/cm<sup>2</sup> bin. Source of ancillary datasets should be configurable for the best dataset. It should be kept in mind that metadata used for the product may be modified, reduced and added in late phase of the product generation.

#### **3.6.3 Quality Assessment and Diagnostics**

The LST retrieval will be assessed and monitored. First, a set of quality control flags will be generated with the LST product for retrieval diagnostics. The quality control flags will indicate the retrieval conditions, including the land/non-land surfaces (i.e., ocean, coast, snow, ice, water etc.), atmospheric water vapor status (i.e., dry, moist and very moist conditions), day and night, large view angle, very cold surface, etc. LST maps and statistical information will be generated and reviewed for quality assessment.

#### **3.6.4 Exception Handling**

The algorithm will handle exceptions through the quality control flags. In calculating the LST for each pixel, quality control flags from input datasets will be examined and skipped for bad sensor data (e.g., missing or no sensor data). Cloudy pixels (i.e., CCF>10%) will also be skipped. Availability of other ancillary datasets such as emissivity and water vapor will also

be checked and the retrieval will be skipped if either is not available. New quality control flags will be generated for indicating the exceptions.

### 3.7 Validation

The algorithm testing described in Section 3.5 is preliminary. More substantial algorithm and product validations are necessary.

The GOES LST system test compared GOES-13 imager retrievals of LST to SURFRAD ground measurements. Test results indicate a retrieval accuracy of 0.8 K and precision of 2.2 K over a measurement range of 260 – 310 K (Fang *et al.*, 2012).

Further validations using the SURFRAD ground measurements and GOES-13 imager data will be performed. First, a two-measurement statistical method developed by Flynn (2007) and Yu *et al.* (2009b) will be applied to analyze statistical features (such as noise and correlation) of the LSTs estimated from the SURFRAD data and from the GOES imager data. Further, a three-measurement method (Yu *et al.* 2009c) will be applied for the accuracy estimation of the LST algorithm. LST diurnal cycle derived using the GOES imager data will be analyzed for assessing the algorithm (Vinnikov *et al.*, 2008). In addition, a ground site characterization study will be performed on the SURFRAD stations for better comparisons between the satellite retrieved LSTs and the ground estimated LSTs.

In addition to using the geostationary satellite data for the algorithm validation, polar orbiting satellite data may also be used for multi-satellite data comparisons. For instances, the Earth Observation Systems (EOS) satellite produces LSTs from its Moderate Resolution Imaging Spectroradiometer (MODIS) data. The multi-satellite data comparison may provide better assessment of the algorithm.

## 4. ASSUMPTIONS AND LIMITATIONS

### 4.1 Assumptions

It is assumed that following data are available before the LST retrieval is performed:

- 1) GSIP L1 data
- 2) GSIP L2 data
- 3) GSIP L3 Snow/ice mask and water vapor dataset
- 4) A high quality dynamic surface emissivity dataset

### 4.2 Limitations

The algorithm described in this document performs in the infrared spectral bands. It is applicable only on cloudless pixels. LST effects due to roughness and/or structure of land surface, the emissivity directional feature and its variation in a pixel are not handled in the algorithm. The retrieved LST value is an effective land surface skin temperature over isothermal mixed pixel. The retrieval accuracy may be reduced significantly in regions with heavy atmospheric water vapor loading (e.g.  $> 5.5 \text{ g/cm}^2$ ). Moreover, the retrieval may be questionable in regions with very low LST and where the surface air temperature is higher than LST.

The current validation effort is limited by comparing LST retrievals at satellite pixel level with ground truth temperature at point level. Due to the heterogeneity of land surface, errors may be introduced by the incompatibility between pixel-sized satellite observations and surface point measurements.

### 4.3 Potential Improvements

#### 4.3.1 Improved Validation Methods

The difficulties with comparison of satellite retrievals with ground observations are well known and common to many other satellite products. They include incompatibility between pixel-sized satellite observations and surface point measurements, unknown error characteristics of ground truth and satellite retrievals and calibration uncertainties in the satellite and ground data.

A method of comparing two data sets (Flynn 2006, Yu et al. 2009b), where both have unknown errors, will be evaluated. The method applies a linear fitting model to the satellite and ground based data and uses the result to estimate precision of both data sets. A related method to make use of three independent observations (Ground observations at SURFRAD, GOES-East and GOES-West) is also being studied (Yu et al., 2011). These methods are expected to allow statistically significant error estimates to be made about each source of data and thereby help specify the error in the satellite LST.

Clearly, the properties of the land surface, specifically land surface cover and emissivity, are very important to its retrieved LST. It is planned to characterize the land surface around the ground truth sites (SURFRAD and CRN) in as much detail as possible. This will help understand differences between the pixel-sized satellite LST and the *in situ* point measurements. High resolution observations, such as the TM (30m) data from landsat, and/or ASTER (90m) data from the Terra satellite, archived at the EROS Data Center will be used in this effort as a bridge of course resolution GOES pixel (4 km) and ground point observations.

### 4.3.2 Algorithm Improvement

The large diurnal variability of LST is something that is conceptually understood, but which is poorly described quantitatively and not explicitly accounted for in the algorithm. The amplitude of the diurnal cycle is determined by surface cover, specifically the green vegetation fraction and soil moisture. The Bowen ratio over bare dry soil is high and over transpiring vegetation is low, and therefore green vegetation fraction in each pixel is important to LST and its diurnal range, with diurnal variation much larger in low vegetation pixels (Sun et al., 2006). A second contributor to LST variation is the fraction of surface shadowing seen from the observing satellite. This effect arises because shaded surfaces are significantly cooler than sunlit surfaces, so the apparent shadow fraction in a pixel is important. It, of course, varies according to the relative geometry of the sun and satellite and is changing throughout daylight hours. All of these factors should be factored into the LST algorithm and work on that problem is planned.

In addition, we are working on an inversion method that can derive the LST and the surface emissivity simultaneously using multi-channel and multi-observation measurements. Originally, such method was applied to the EOS/MODIS mission through its day and night observations over a pixel (Wan et al., 1997). The method can be applied to GOES Imager data better since it provides multiple observations over a pixel in a short time interval, which ensures constant emissivity during the time which is the baseline of the inversion method. We simplified the method significantly and have had the output stable and faster (Yu et al., 2009d; Fang et al., 2010).

### 5. LIST OF REFERENCES

Aminou, D., and coauthors, "Meteosat Second Generation: A comparison of on-ground and on-flight imaging and radiometric performances of SEVIRI on MSG-1," *Proceedings of 'The 2003 EUMETSAT Meteorological Satellite Conference', Weimar, Germany, 29 September – 3 October 2003*, pp. 236–243, 2003.

Augustine, J. A., J. J. DeLuisi, C. N. Long, "SURFRAD- A National Surface Radiation Budget Network for Atmospheric Research", *Bull. Amer. Meteor. Soc.*, 81, 2341-2357, 2000.

Augustine, J. A., G. B. Hodges, C. R. Cornwall, J. J. Michalsky and C. I. Medina, "An Update on SURFRAD- The GCOS Surface Radiation Budget Network for the Continental United States", *J. Atmos. Oceanic Technol.*, 22, 1460-1472, 2005.

Becker, F., and Z. L. Li., "Towards a local split window method over land surfaces", *Int. J. Remote Sensing*, vol. 11, pp. 369-393, 1990.

Berk, A., G. P. Anderson, P. K. Acharya, J. H. Chetwynd, M. L. Hoke, L. S. Bernstein, E.P. Shettle, M.W. Matthew and S.M. Alder-Golden , *MODTRAN4 Version 2 Users's Manual*, Space Vehicles Directorate, Hanscom AFB, MA 01731-3010, April 2000.

Breiman, L., J. H. Friedman, R. A. Olshen, and C. J. Stone, "Classification and Regression Trees", Wadsworth & Brooks/Cole Advanced Books & Software, Pacific Grove, CA, 1984. Borbas, E. E., L. Moy, S. W. Seemann, R. O. Knuteson, P. Antonelli, J. Li, H-L Huang, I. Trigo, I. de Meteorologia, L. Zhou, "A global infrared land surface emissivity database and its validation" P2.7, AMS Annual meeting, New Orleans, January, 2008.

Caselles, V., C. Coll, and E. Valor, "Land surface temperature determination in the whole Hapex Sahell area from AVHRR data," *Int. J. Remote Sens.*, vol. 18, no. 5, pp. 1009–1027, 1997.

Coll, C., E. Valor, T. Schmugge, and V. Caselles, "A procedure for estimating the land surface emissivity difference in the AVHRR channels 4 and 5," *Remote Sensing Application to the Valencian Area, Spain*, 1997.

De'ath, G. and K. E. Fabricius, "Classification and regression trees:a powerful yet simple technique for ecological data analysis.", *Ecology*, 81(11), 3178-3192, 2000.

Ellrod, G. P., Detection and analysis of fog at night using GOES multispectral infrared imagery, NOAA Tech. Rep. NESDIS 75, 22 pp., 1998.

EUMETSAT homepage,  
[http://www.eumetsat.int/groups/ops/documents/document/pdf\\_ten\\_052562\\_msg1\\_spcctrsp.pdf](http://www.eumetsat.int/groups/ops/documents/document/pdf_ten_052562_msg1_spcctrsp.pdf).

Fang, L., Liu, Y., Sun, D., Jensen, K., and Yu, Y., "GOES LST Verification and Validation Report", 2012

Flynn, L., "Comparisons Two Sets of Noisy Measurements", NOAA Technical Report, NESDIS Office of Research and Applications, 2006.

Gallo, K. P., T. W. Owen, D. R. Easterling, Temperature trends of the U.S. historical climatology network based on satellite-designated land use/land cover, *J. Clim.* 12, no. 5, pp. 1344-1348, 1999.

Han, J. and M. Kamber, "Data Mining: Concept and Techniques", Morgan Kaufmann Publishers, San Francisco, CA, 284-290, 2001.

Hansen, M., and B. Reed, "A comparison of the IGBP DISCover and University of Maryland 1 km global land cover products", *International Journal of Remote Sensing* 21 (2000) (6-7), pp. 1365-1373, 2000.

Hillger, D., W. Ellrod, P. Gary, Detection of Important Atmospheric and Surface Features by Employing Principal Component Image Transformation of GOES imagery, *Journal of Applied Meteorology*, Vol. 42, No. 5, pp. 611-629, 2003.

Li, Z-L, and F. Becker, Feasibility of land surface temperature and emissivity determination from AVHRR data, *Remote Sensing of Environment*, vol. 43, pp. 67-85, 1993.

Jin, M., and S. Liang, "An improved land surface emissivity parameter for land surface models using global remote sensing observations", *J. Climate*, 19, 2867-2881.

Karl, T. R. , P. D. Jones, R. W. Knight, G. Kukla, N. Plummer, V. Razuvayev, K. P. Gallo, J. Lindsey, R. J. Charlson, T. C. Peterson, A new perspective on recent global warming, *Bull. Am. Meteorol. Soc.* 74, pp. 1007-1023, 1993.

McMillin, L. M., "Estimation of sea surface temperatures from two infrared window measurements with different absorption", *Journal of Geophysical Research* 80 (C36), pp. 5113-5117, 1975.

McMillin, L. M., and D. S. Crosby, "Theory and validation of multiple window sea surface temperature technique", *J. Geophys. Res.*, 89, 3655-3661, 1984.

Menzel, W. P., and J. F. W. Purdom, Introducing GOES-I: The First of a New Generation of Geostationary Operational Environmental Satellites, *Bull. Amer. Meteor. Soc.*, 75, 757-781, 1994.

Norman, J. M., and F. Becker, Terminology in thermal infrared remote sensing of natural surfaces, *Remote Sensing Rev.* 12:159-173, 1995.

Peterson, T. C., Assessment of urban versus rural in situ surface temperature in the contiguous United States: No difference found, *J. Clim.* 16, no. 18, pp. 2941-2959, 2003.

Prata, A. J., and C. M. R. Platt, "Land surface temperature measurements from the AVHRR," in Proc. 5th AVHRR Data Users Conf., Tromso, Norway, Jun. 25–28, pp. 438–443. EUM P09, 1991.

Prata, A. J., "Land surface temperatures derived from the AVHRR and the ATSR, 1, Theory," J. Geophys. Res., 98(D9), 16,689–16,702. 1993.

Prata, A. J., "Land surface temperatures derived from the AVHRR and the ATSR, 2, Experimental results and validation of AVHRR algorithms," J. Geophys. Res., 99(D6), 13,025–13,058. 1994.

Price, J. C., "Land surface temperature measurements from the split window channels of the NOAA-7/AVHRR", J. Geophys. Res., vol. 89, pp. 7231–7237, 1984.

Schmetz J, Pili P, Tjemkes S, Just D, Kerkmann J, Rota S, Ratier A., "An introduction to Meteosat Second Generation (MSG)", *Bulletin of the American Meteorological Society*, 83, 977-992, 2002.

Schmid J, "The SEVIRI Instrument", Proceedings of the 2000 EUMETSAT Meteorological Satellite Data User's Conference, Bologna, Italy, 29 May – 2 June 2000, 2000.

Schmit T. J., W. F. Feltz, W. P. Menzel, J. Jung, A. P. Noel, J. N. Heil, J. P. Nelson III, G. S. Wade, "Validation and use of GOES sounder moisture information", *Wea. Forecasting*, 17, 139-154, 2002.

Schmit, T.J., J. Li, M.M. Gunshor, C.C. Schmidt, W.P. Menzel, J. Gurka, and J. Sieglaff, Study of the Advanced Baseline imager (GOES IMAGER) on the GOES-R and beyond, 84<sup>th</sup> AMS Annual Meeting, Seattle WA, 2004.

Schmit, T. J., W. Paul Menzel, J. Gurka, M. Gunshor, "The GOES IMAGER on GOES-R, 3rd Annual Symposium Future National Operational Environmental Satellite Systems", San Antonio, January 16, 2007.

Schumann W, Stark H, McMullan K, Aminou D, Luhmann H-J., "The MSG System", *ESA bulletin*, 111, 2002.

Sellers, P. J., F. G. Hall, G. Asrar, D.E Strebel, and R. E. Murphy, The first ISLSEP field experiment (FIFE), *Bull. Amer. Meteorol. Soc.*, Vol. 69, no. 1, 22-27, 1998.

Sikorski, R. J., P.S. Kealy, and W. J. Emery, Land Surface Temperature Visible/Infrared Image radiometer Suite Algorithm Theoretical Basis Document, Version 5, Raytheon Systems Company, 2002. Available: <http://npoesslib.ipo.noaa.gov/atbd/viirs/>.

Snyder, W. C., Z. Wan, and Y. Z. Feng, "Classification-based emissivity for land surface temperature measurement from space", *Int. J. Remote Sensing*, vol. 19, no. 14, pp. 2753-2774, 1998.

Sobrino, J. A., Z. L. Li, M. P. Stoll, and F. Becker, "Improvements in the split-window technique for land surface temperature determination," *IEEE Trans. Geosci. Remote Sens.*, vol. 32, no. 2, pp. 243–253, Mar. 1994.

Sobrino, J. A., Z. L. Li, M. P. Stoll, and F. Becker, "Determination of the surface temperature from ATSR data," in *Proc. 25th Int. Symp. Remote Sens. Environ.*, Graz, Austria, Apr. 4–8, pp. II-19–II-109, 1993.

Sun D. and Y. Yu, 2010: Deriving *water fraction* and flood map with the EOS/MODIS data using regression tree approach. ISPRS 100-year Commission VII Symposium, Vienna, 2-7 July 2010.

Sun, D. and Pinker, R.T. Estimation of land surface temperature from a Geostationary Operational Environmental Satellite (GOES-8). *Journal of Geophysical Research, D, Atmospheres* v.108, no. D11, 3 June 2003. S

Sun, D., and R. Pinker, "Case study of soil moisture's effect on land surface temperature retrieval", *IEEE Trans. Geos. Remote Sens. Lett.*, 1 (2), 127-130, 2004.

Sun, D. L., R. T. Pinker, J. B. Basara, Land surface temperature estimation from the next generation of Geostationary Operational Environmental Satellites: GOES M-Q, *J. Appl. Meteorol.* 43, pp. 363-372, 2004.

Sun, D. L., R. T. Pinker, M. Kafatos, Diurnal temperature range over the United States: A satellite view, *Geophys. Res. Lett.* 33, pp. L05705, 2006. [doi:10.1029/2005GL024780](https://doi.org/10.1029/2005GL024780).

Ulivieri, C., and G. Cannizzaro, "Land surface temperature retrievals from satellite measurements," *Acta Astronaut.*, vol. 12, no. 12, pp. 985–997, 1985.

Ulivieri, C., M. M. Castronovo, R. Francioni, and A. Cardillo, "A SW algorithm for estimating land surface temperature from satellites," *Adv. Space Res.*, vol. 14, no. 3, pp. 59–65, 1992.

Vidal, A., "Atmospheric and emissivity correction of land surface temperature measured from satellite using ground measurements or satellite data," *Int. J. Remote Sens.*, vol. 12, no. 12, pp. 2449–2460, 1991.

Vinnikov, K. Y., Y. Yu, M. K. Rama Varna Raja, D. Tarpley, M. Goldberg, "Diurnal-seasonal and weather-related variations of land surface temperature observed from geostationary satellites", *Geophys. Res. Lett.*, **vol. 35**, L22708, [doi:10.1029/2008GL035759](https://doi.org/10.1029/2008GL035759), 2008.

Walton, C. C., Pichel, W. G., Sapper, J. F., and May, D. A., "The development and operational application of non-linear algorithms for the measurement of sea surface temperatures with the NOAA polar-orbiting environmental satellites", *Journal of Geophysical Research*, 103, 27 999–28 012, 1998.

Wan, Z., and J. Dozier, "A generalized split-window algorithm for retrieving land-surface temperature measurement from space", *IEEE Trans. Geosci. Remote Sensing*, vol. 34, pp. 892–905, 1996.

Wan, Z., and Z. Li, "A physics-based algorithm for retrieving land-surface emissivity and temperature from EOS/MODIS data", *IEEE Trans. Geosci. Remote Sens.*, **35**, 980–996, 1997.

Wan, Z., "MODIS Land-Surface Temperature Algorithm Basis Document (LST ATBD): version 3.3," (April 1999).

Wang, Y. and I. H. Witten, 1997: Induction of model trees for predicting continuous classes. Poster papers of the 9th European Conference on Machine Learning, 1997.

Yu, Y., and I. J. Barton, "A non-regression-coefficients method of sea surface temperature retrieval from space", *Int. J. Rem. Sens.*, 15, 1189-1206, 1994.

Yu, Y., J. L. Privette, and A. C. Pinheiro, "Analysis of the NPOESS VIIRS land surface temperature algorithm using MODIS data," *IEEE Trans. Geosci. Remote Sens.*, vol. 43, no. 10, pp. 2340–2350, Oct. 2005.

Yu, Y., Ana C. Pinheiro, J L. Privette, "Correcting land surface temperature measurements for directional emissivity over 3-D structured vegetation", SPIE San Diego , July, 2006.

Yu, Y., J. P. Privette, and A. C. Pinheiro, "Evaluation of split window land surface temperature algorithms for generating climate data records", *IEEE Trans. Geosci. Remote Sensing*, vol. 46, No. 1, pp. 179-192, 2008.

Yu, Y., D. Tarpley, J. L. Privette, M. K. Rama Varna Raja, K. Vinnikov, H. Xue, "Developing algorithm for operational GOES-R land surface temperature product", *IEEE Trans. Geosci. Remote Sens.*, **vol. 47**, no. 3, pp. 936-951, 2009a.

Yu, Y., D. Tarpley, J. L. Prrivette, L. Flynn, H. Xu, M. Chen, K. Vinnikov, and D. Sun, "Towards Satellite Land Surface Temperature Validation Using SURFRAD Ground Measurements", *IEEE Trans. Geosci. Remote Sens.*, in revision, 2011.

Yu, Y., M. Chen, K. Vinnikov, D. Tarpley, and H. Xu, "A Three-measurement Model Developed for Evaluating Satellite Land Surface Temperature Product", SPIE 2009, San Diego, 2009c.

Yu, Y., H. Xu, D. Tarpley, and M. Goldberg, "A Simplified method for measuring land surface temperature and emissivity using thermal infrared split-window channels", IGARSS 2009, Proc., Cape Town, 2009d.

---

# NOAA NESDIS STAR

ALGORITHM THEORETICAL BASIS DOCUMENT

Version: 1.0

Date: January 17, 2012

TITLE: GOES LST Algorithm Theoretical Basis Document

Page 82 of 81

---

END OF DOCUMENT